2018-11-23

Distributed Electric Propulsion Conceptual Design Applied to Traditional Aircraft Take Off Distance Through Multidisciplinary Design

Kevin Ray Moore
Brigham Young University

Distributed Electric Propulsion Conceptual Design Applied to Traditional Aircraft Takeoff Distance Through Multidisciplinary Optimization

Kevin Ray Moore

A thesis submitted to the faculty of
Brigham Young University
in partial fulfillment of the requirements for the degree of

Master of Science

Andrew Ning, Chair
Scott L. Thomson
Steven E. Gorrell

Department of Mechanical Engineering

Brigham Young University

ABSTRACT

Distributed Electric Propulsion Conceptual Design Applied to Traditional Aircraft Takeoff Distance Through Multidisciplinary Optimization

Kevin Ray Moore
Department of Mechanical Engineering, BYU
Master of Science

While vertical takeoff and landing aircraft show promise for urban air transport, distributed electric propulsion on existing aircraft may offer an immediately implementable alternative. Distributed electric propulsion has the potential of increasing the aircraft thrust-to-weight ratio and lift coefficient high enough to enable takeoff distances of less than 100 meters. While fuel based propulsion technologies generally increase in specific power with increasing size, electric propulsion typically can be decreased in size without a decrease in specific power. The smaller but highly power-dense propulsion units enable alternative designs including many small units, optionally powered units, and vectored thrust from the propulsion units, which can all contribute to better runway performance, decreased noise, adequate cruise speed, and adequate range. This conceptual study explores a retrofit of continuously powered, invariant along the wingspan, open bladed electric propulsion units. To model and explore the design space we used a set of validated models including a blade element momentum method, a vortex lattice method, linear beam finite element analysis, classical laminate theory, composite failure, empirically-based blade noise modeling, motor mass and motor controller empirical mass models, and nonlinear gradient-based optimization. We found that while satisfying aerodynamic, aerostructural, noise, and system constraints, a fully blown wing with 16 propellers could reduce the takeoff distance by over 50% when compared to the optimal 2 propeller case. This resulted in a conceptual minimum takeoff distance of 20.5 meters to clear a 50 ft (15.24 m) obstacle. We also found that when decreasing the allowable noise to 60 dBa, the fully blown 8 propeller case performed the best with a 43% reduction in takeoff distance compared to the optimal 2 propeller case. This resulted in a noise-restricted conceptual minimum takeoff distance of 95 meters.Takeoff distances of this length could open up thousands of potential urban runway locations to make a retrofit distributed electric aircraft an immediately implementable solution to the urban air transport challenge.

Keywords: distributed electric propulsion, aircraft design optimization, propeller aerostructural design

ACKNOWLEDGMENTS

I would like to thank my graduate advisor, Dr. Andrew Ning, for his support, trust, and enabling leadership methods. I would like to thank the excellent mechanical engineering laboratory faculty including Kevin Cole, Nick Hawkins, and Dave Laws for their real world experience and advice. I would like to thank my colleagues in the FLOW lab for their insight, help, and the amazing collaborative learning environment. I gratefully acknowledge support from The Connectivity Lab at Facebook. And finally, I would like to acknowledge and thank my beautiful wife, Bethany, for her unwavering patience and support during this entire process.

TABLE OF CONTENTS

LIST OF TABLES . . . . . **vi**

LIST OF FIGURES . . . . . **viii**

Chapter 1 Introduction **1**
1.1 Conceptual Aircraft Design 1
1.2 Distributed Electric Propulsion 2
1.3 Contribution 5
1.4 Thesis Outline 6

Chapter 2 Model Description **7**
2.1 Atmosphere 7
2.2 Propeller Aerodynamics 8
2.2.1 Airfoil Pre-computation 11
2.2.2 Propeller Performance Comparison 14
2.3 Propeller Noise 14
2.4 Composite Structures 18
2.4.1 Propeller Blade Composite Layup 19
2.4.2 Linear Finite Element Analysis 20
2.4.3 Composite Frame of Reference Stress 21
2.4.4 Material Properties 22
2.4.5 Material Failure 23
2.4.6 Aerostructural Verification 24
2.5 Waked Wing Modeling 27
2.5.1 Prop on Wing Smoothing 29
2.5.2 Propeller on Wing Validation 32
2.6 Electric Components Modeling 33
2.6.1 Electric Motor 33
2.6.2 Linearized Battery and Motor Controller Masses 35

Chapter 3 Aircraft Takeoff Performance **37**
3.1 Ground Roll Distance / Acceleration 38
3.2 Steady Climb 38
3.3 Transition 39
3.4 Range 40

Chapter 4 Optimization Setup **41**
4.1 Optimization Algorithm 42
4.1.1 Problem-Specific Optimization Techniques 43
4.2 Framework 45
4.3 Baseline Aircraft 47

Chapter 5 Results **49**
5.1 Cruise Speed Sweep 49
5.1.1 Augmented Thrust 51
5.1.2 Augmented Lift 53
5.1.3 Acceleration Time 54
5.1.4 Example Propeller Design 55
5.2 Noise Constraint Sweep 57
5.2.1 Noise Constrained Thrust 58
5.2.2 Noise Constrained Lift Coefficient 59

Chapter 6 Summary **61**
6.1 Conclusions 62
6.2 Future Work 63
6.3 Code 64

REFERENCES **65**

Appendix A Steady Climb Tradeoff Study **71**

LIST OF TABLES

2.1 Composite Material Properties 22
2.2 Material Scatter Knockdown Factors 23
2.3 Blade Skin Stacking Sequence. 26

4.1 Optimization Design Variables and Bounds 47
4.2 Baseline Tecnam p2006t aircraft [69] 48

LIST OF FIGURES

1.1 Illustration of the NASA X-57 thin-haul concept aircraft showing the mid span DEP propellers in the folded cruise position. 3
1.2 NASA conceptual vision of the urban air taxi concept. (Image reprinted from "NASA Embraces Urban Air Mobility, Calls for Market Study", by L. Gipson, 2017, Retrieved from https://www.nasa.gov/aero/nasa-embraces-urban-air-mobility. Public Domain Credit: NASA) 4

2.1 The blue streamtube depicts an annular control volume used in blade element momentum theory including the oncoming freestream (V_x) at the upstream plane (∞), the rotor plane (2 and 3), and the far wake (w) with a representation of the wake contraction. . . 9
2.2 Validation of 3D rotational stall correction with experimental data from [33] for two different chord to radius c/r ratios of the FFA airfoil on the STORK 5 WPX wind turbine. 12
2.3 Extrapolated E212 airfoil data using the Viterna airfoil extrapolation method. Xfoil data ranges from approx. -10 to 20 degrees AOA with the Viterna airfoil extrapolation method for the remaining range of AOA. 13
2.4 Comparison of propeller efficiency with data collected by Epema [30] and the BEM code using XFOIL airfoil data. A maximum error of 5% can be seen in the normal regions of operation which are the advance ratios below which the steep drop off occurs. 15
2.5 Noise profile of example 8 propeller case in climb at 50 ft with respect to a ground observer. (Airframe included for reference.) 16
2.6 Propeller noise contours comparing a case with only tip speed changes (representative of using propeller tip speed as a surrogate for noise) and a case representative of propeller design changes as the number of propellers is increased for a DEP STOL system. Tip speed alone is not an adequate measure to compare designs. 17
2.7 Power-to-noise ratio further illustrating the non-uniform tradeoffs between propeller design and noise. 18
2.8 E212 Airfoil shell composite layup. 19
2.9 Precomp reference axes and centers. (Image reprinted from "Users Guide to PreComp", by G. Bir, 2005, Retrieved from https://nwtc.nrel.gov/PreComp. Copyright 2005 National Renewable Energy Laboratory. 20
2.10 Composite sections of the SNL 61.5 m wind turbine for airfoil geometry at 30.0 m span. From left to right: trailing edge (te), reinforced trailing edge thicknesses (te-reinf), trailing edge panel (te-panel), first shear web (web 1), reinforced spar cap (cap), second shear web (web 2), leading edge panel (le-panel), and leading edge (le). 25
2.11 Composite thicknesses for the SNL 61.5 meter wind turbine blade. Dots are data as extracted from Resor's report [48] and lines correspond to the splined values used. . . . 25
2.12 Comparison of mass distribution and flap-wise bending stiffness for the SNL 61.5 m wind turbine. Present study in blue, SNL in green, and NREL in red. 26
2.13 Graphical strain contour of the Sandia National Labratories 61.5 wind turbine created using our aerostructural framework. Reported strain matches within 5% while composite stresses and buckling were within the reported safety margins. 27

2.14 A representation of the strategy used to evaluate changing rotor diameters. Rotor wake is oversized to fit in the blue, then undersized to fit in the red, then the resulting analyses are linearly interpolated to the actual rotor wake (shaded grey). Viscous drag is also included in the interpolation allowing for partial waking of the VLM panels for the viscous model as well 30
2.15 A comparison between the original VLM output and our modified approach with changing rotor diameter. As the propeller diameter changes, the propeller wake discretely intersects with wing control points creating noisy output. Our modified approach allows for smooth variations with changing propeller diameter. The lift coefficient is shown on a smaller x-axis range because the oscillations are smaller and are harder to see when zoomed out. 31
2.16 Two validation cases for propeller on wing interaction using two different geometries. . 32
2.17 Electric motor equivalent circuit. 33
2.18 Data fits based on Astroflight motor data. 35

3.1 Example takeoff profile scaled to represent a sample 8 propeller case. Takeoff transition becomes significant when the flight path angle is greater than a few degrees. . . . 37

4.1 Number of function evaluations required to converge optimization as a function of number of design variables. Sparse Nonlinear OPTimizer is used for the gradient-based results and Augmented Lagrangian Particle Swarm Optimizer for the gradient-free results, however similar trends were observed using Sequential Least SQuares Programming (gradient-based) and Non Sorting Genetic Algorithm II (gradient-free). Reference lines for linear and quadratic scaling are also shown. (Image and caption reprinted from "Integrated Design of Downwind Land-based Wind Turbines using Analytic Gradients", by A. Ning, 2016, Wind Energy, 11, 44. Copyright 2016 John Wiley & Sons, Ltd.) 42
4.2 Optimization framework with design variables in red, models in green, and outputs in blue. For the multi objective optimization of takeoff distance and cruise speed, we added a speed constraint and ran the analysis framework three times with additional variables for angle of attack, pitch, RPM, and velocity for the cruise and two takeoff parts. 46

5.1 Cruise speed and number of propellers effect on optimal takeoff distance to clear a 50 ft obstacle. The 16 propeller case achieves the takeoff distance in less than half that of the 2 propeller case for the cruise speed requirements tested. Greater-than symbol indicates cruise speed constraint was not active. 50
5.2 Cruise speed and number of propellers effect on resulting ground roll distance. 51
5.3 Tradeoff between battery mass and propulsion mass, or ability to generate thrust. With MTOW constraint active, propulsion mass must be reduced to allow for extra battery mass to maintain range at the expense of takeoff potential. 52

5.4 Wing lift coefficient in the climb state with an assumed maximum local lift coefficient of 2.4 as a surrogate for extended flaps with a zero lift angle of attack at -14 deg for a single slotted flap with 30 deg deflection [56]. Fully blown configurations increase wing total lift coefficient as normalized by the freestream, though for the highly mass constrained systems, blown velocities and in turn lift coefficient is also constrained due to undersized propulsion systems. 53
5.5 Time duration for takeoff maneuvers is on the same order of magnitude as a 1 second operator reaction time [60]. 54
5.6 Single propeller from the 8 propeller, 45 m/s cruise case with the composite weave failure scaled constraint contour on the upper blade and the buckling failure scaled constraint contour on the lower blade. Constraints are active when zero or positive. Calculated noise for this case was unconstrained and at 71 dBa 55
5.7 Visual depiction of optimal rotor diameters relative to wingspan for the 45 m/s cruise case. For more than 8 propellers, the blades are effectively tip-to-tip across the span. . 56
5.8 Noise constraint effects on optimal takeoff distance with varying numbers of propellers. Decreasing the propeller noise constraint significantly increases takeoff distance. This analysis differs from section 5.1 with a fixed 45 m/s cruise speed constraint and varying propeller noise constraint. Less-than symbol indicates noise constraint was not active 58
5.9 Noise constraint effects on thrust and augmented lift. Decreasing noise allows for less thrust, less induced velocity, and in turn less lift augmentation. 59
5.10 Takeoff distance for the 16 propeller, 45 m/s cruise case with varying noise constraint shows relatively small effect on performance for noise levels between 71 and 65 dBa. . 60

A.1 Thrust is the major factor when determining the flight path angle. Increasing lift coefficient increases the induced drag which decreases the net thrust. 72
A.2 Lift coefficient plays a significant role in the power required for a given flight path angle. Increasing from 0.4 to 1.4 halves the amount of power required for a 45 degree flight path angle. 73
A.3 Increasing the lift coefficient decreases total energy for the climb until the maximum net power is achieved. A lift coefficient of 0.6 is the best for the cases shown here. . . . 73

CHAPTER 1. INTRODUCTION

Aircraft are the basis for fast, long distance travel. We rely on them for transport, delivery, military operations, recreation, and a significant part of the world economy. Recently, electric air vehicles have become of significant public interest with new companies emerging every year in the areas of urban air transportation, thin-haul aircraft commuter, and unmanned aerial package delivery. Distributed electric propulsion (DEP), or many small propulsion units spread across an aircraft wing, has shown promise in harnessing the advantages of electric systems while minimizing their weaknesses. This technology may be able to make an urban air transport system feasible by satisfying the required intra-city operating constraints of takeoff distance, cruise speed, range, noise, and safety. The purpose of this thesis is to give conceptual insight into using DEP on traditional aircraft to shorten takeoff distance while satisfying the operating requirements that would enable the technology to serve as an alternative to vertical takeoff and landing aircraft for urban air transport.

This chapter includes a brief overview of DEP system theory and aircraft conceptual design optimization. This chapter also includes a review of previous work and what contributions this thesis has made.

1.1 Conceptual Aircraft Design

Conceptual aircraft design is a process that enables large systems to be analyzed at their fundamental levels to avoid the cost of iterative detailed design where large changes will be prohibitively expensive [1]. Highly coupled designs, such as the aerodynamic, structural, and propulsion system included in DEP, require system level factors to be accounted for where they may have previously been neglected. Electric systems, though highly power dense, suffer from the very low energy density of the battery storage. A fuel based system has approximately 8 times the energy

capacity per weight after being converted to mechanical power. Because of this low energy storage, changes in efficiency of the propulsion system and wing have large effects on mass, which circularly compounds due to the coupled physics. By modeling all of the components and interactions at the fundamental level, we can address those tradeoffs and give a much better starting point for detailed design requiring fewer final design iterations.

1.2 Distributed Electric Propulsion

In early aircraft designs, distributed propulsion was used more out of necessity than deliberate choice. Designs such as the Dornier Do X in 1929, the Hughes H-4 Hercules in 1947, and many other large aircraft before the jet age, were constrained by the available propulsion units of the time [2]. With the dawn of the jet age, aircraft began to use fewer but engines. However, some distributed and blended wing jet concepts were explored as early as 1954 [3]. During the push for high altitude long endurance (HALE) aircraft design, distributed electric propulsion (DEP) emerged as a viable option with NASA's Pathfinder in 1983 [4]. In 1988, NASA produced several concepts including distributed propulsion with the intention of lift augmentation [5], which evolved until the Helios' destruction in 2003 [6]. In the 2000s, a third wave of aeronautics began to emerge, termed by NASA as on demand mobility (ODM) [7], or unscheduled aircraft services. Within ODM, two applications have begun to be targeted: thin-haul commuters and urban air taxis [8].

Thin-haul commuters, the first ODM application, are aircraft designed to fly routes not justifiable by large airlines. An example concept emerged in 2014 when NASA partnered with Joby Aviation and Empirical Systems Aerospace to use the Leading Edge Asynchronous Propeller Technology (LEAPTech) as a test bed for distributed propulsion research [9]. Additionally, in 2016, NASA announced the X-57 Maxwell short haul commuter (see fig. 1.1) with goals to reduce the energy required for cruise by 4.8x without sacrificing cruise speed or takeoff distance [10]. Since the X-57, there has been a significant increase in the amount of research regarding DEP for thin-haul commuters in areas such as economics [11], multidisciplinary modeling requirements [12], wing aerodynamic analysis [9, 10, 13], motor design [14], avionics [15], hybrid propulsion [16],

Figure 1.1: Illustration of the NASA X-57 thin-haul concept aircraft showing the mid span DEP propellers in the folded cruise position. (Image reprinted from "NASA Electric Research Plane Gets X Number, New Name", by A. Beutel, 2017, Retrieved from https://www.nasa.gov/press-release/nasa-electric-research-plane-gets-x-number-new-name. Public Domain Credit: NASA)

trajectory thermal considerations [17], certification and landing safety [18] and large scale multi-disciplinary optimization of design and trajectory [8].

Urban air taxis, the second ODM application, are aircraft designed for 2-6 passengers and distances less than 100 miles [19]. Though there is significant infrastructure required to adopt this type of transportation, there is potential for competitive operating costs [20]. The economic possibilities have driven the development of a variety of concepts including tilt rotor, multi-rotor, and tilting ducted fans. The concept of urban air transport with conventional small fixed-wing aircraft as opposed to vertical takeoff and landing aircraft has been previously explored [21]. However, the concept of using distributed electric propulsion to shorten the runway distance is relatively recent. In the predecessor to this work [22], we used a propeller-on-wing aerodynamic model and electric component performance modeling to show an 80% reduction in takeoff rolling distance

Figure 1.2: NASA conceptual vision of the urban air taxi concept. (Image reprinted from "NASA Embraces Urban Air Mobility, Calls for Market Study", by L. Gipson, 2017, Retrieved from https://www.nasa.gov/aero/nasa-embraces-urban-air-mobility. Public Domain Credit: NASA)

using an optimal distributed electric propulsion design as opposed to an optimal two-propeller electric configuration. More recently, Courtin et al. [23] conducted a feasibility analysis of the STOL concept for on urban air transport with the geometric programming (GP) method. They took a broad approach to the STOL urban air transport problem including takeoff rolling distance, landing distance, wing spar sizing using root bending moment, propulsion effects via 2D jets, and lift augmentation using a momentum balance. According to the study, runway lengths need only be less than 150 m (500 ft) to have feasible DEP aircraft access to thousands of potential locations in cities such as Dallas and Chicago.

In our study, we propose to extend the benefits of DEP on a fixed wing similar to the X-57 to explore short takeoff and landing (STOL) fixed wing aircraft as a potential alternative concept for the urban air taxi. As discussed by Courtin et al., this type of air vehicle could decrease the difficulty of FAA certification, potentially address noise concerns, and offer a more fail safe approach due to the fixed wing nature and redundancy of many individual propulsion units.

1.3 Contribution

The area of STOL DEP fixed wing aircraft applied to urban air transport is a new and emerging topic with little research applied specifically to the subject. However, the principles of DEP applied to a fixed wing aircraft for a thin-haul commuter apply to the STOL urban air transport with the main difference being the required runway and cruise performances. While there are many remaining technical challenges relating to DEP applied to fixed wing aircraft in areas such as wing stall, safety through redundancy, and higher fidelity design optimization, we focus on exploring the conceptual abilities of DEP applied to the urban transport problem.

This thesis builds upon previous work by exploring the STOL urban transport problem with greater detail including the associated aerodynamic, structural, design, and noise constraints. This is done with higher fidelity propulsion aerostructural analysis, component mass estimation, and component power models as well as propeller on wing interaction, blown viscous and induced drag, takeoff transition and climb, and blade noise modeling. The study presented here contributes to the STOL DEP urban air transport problem in five fundamentally important ways.

- First, we include the full propeller design including chord, twist, and composite structure.
- Second, we model propeller noise including tip vortex and boundary layer vortex shedding, tip and trailing edge turbulence, and trailing edge bluntness.
- Third, we present a new method for smooth gradients with respect to propeller radius and propeller on wing interactions.
- Fourth, we model the full takeoff consisting of ground roll, transition, and climb to overcome a 50 ft obstacle.
- Fifth, to make the study more immediately relevant, we make the case of a conceptual propulsion-only retrofit to the existing Tecnam p2006t, an aircraft already in process of exchanging the fuel based propulsion for an electric system [24].

1.4 Thesis Outline

This first chapter introduced distributed electric propulsion at the fundamental level as applied to aircraft conceptual design optimization. The second chapter addresses models relating to propeller and wing aerodynamics, propeller noise, propeller aerostructural, and electrical component modeling. The third chapter focuses on aircraft performance, specifically modeling the takeoff, transition, climb, and cruise. The fourth chapter summarizes the optimization setup and baseline configuration. The fifth chapter presents results for the short takeoff retrofit aircraft. Finally, the sixth chapter concludes the work with a brief review of findings and suggestions for future work.

CHAPTER 2. MODEL DESCRIPTION

In this section, models relating to propeller and wing aerodynamics, propeller noise, propeller aerostructural, and electrical component modeling are outlined. These include atmospheric modeling, blade element momentum theory, airfoil preprocessing, BPM (Brooks, Pope, and Marcolini) noise modeling, composite structures, vortex lattice method, propeller on wing interaction modeling, electric motor performance and mass, motor controller mass, and battery mass. Several verification and validation cases are also presented.

2.1 Atmosphere

We model the atmospheric properties using NASA's 1976 Standard Atmosphere Model[1] [25]. Since the framework was originally intended to be generalized to allow for possible future applications we included this full atmospheric model. This model is comprised of extensive rocket data for altitudes above 50 km, satellite data for the thermosphere, and ideal gas theory for the mesosphere and lower thermosphere. A continuous fit to the data, as done by Drela [26], for temperature T in Kelvin and pressure P in Pascals is shown in eqs. (2.1) and (2.2) with the height h in kilometers and the subscript sl indicating sea level values.

$$T = T_{sl} - 71.5 + 2log\left(1 + e^{35.75-3.25h} + e^{-3.0+0.0003h^3}\right) \tag{2.1}$$

$$P = P_{sl}\, e^{-0.118h - \frac{0.0015h^2}{1-0.018h+0.0011h^2}} \tag{2.2}$$

From the temperature and pressure, we can use Ideal Gas Law to calculate density and speed of sound. As shown in eq. (2.3), the air density ρ is calculated from the pressure and

[1] BYU FLOW Lab GitHub Atmosphere.jl https://github.com/byuflowlab/Atmosphere.jl.git

temperature calculated previously, and the molar gas constant R_M of 287.052 for air. The speed of sound a in eq. (2.4) is calculated in a similar fashion using Ideal Gas Law including the ratio of specific heats γ of 1.4.

$$\rho = \frac{P}{R_M T} \tag{2.3}$$

$$a = \sqrt{\gamma R_M T} \tag{2.4}$$

To calculate dynamic viscosity μ, Sutherland's equation is used as shown in eq. (2.5) with the temperatures at sea level and at the flight altitude, as well as Sutherland's constant S_c of 113.0 Kelvin for air.

$$\mu = \mu_{sl}\left(\frac{T}{T_{sl}}\right)^{\frac{3}{2}}\frac{T_{sl}+S_c}{T+S_c} \tag{2.5}$$

2.2 Propeller Aerodynamics

CCBlade is an open source blade element momentum (BEM) code originally designed for wind turbine analysis [27], but which has been extended for propeller analysis including all possible inflow angles, large axial inductions, hover, and non-rotating blades.[2] The non-normal inflow correction allows us to mount the props in line with the wing and include the angle of attack (AOA) of the wing as the inflow angle to the prop. In conjunction with 2D airfoil data corrected for rotational stall, the blade element momentum method converts the 2D lift and drag coefficients into the 3D blade frame of reference, solving for the distributed thrust and torque. This particular version of the blade element momentum method is formulated to give guaranteed convergence and in turn allow for a continuously differential output across wide potential operating conditions. In BEM, to solve for the local inflow angle and relative angles of attack at each blade section due to the induced axial and tangential velocity, an iterative or residual approach must be taken. Equation (2.6) shows the residual equation used in this formulation with the local inflow angle

[2]CCBlade.jl on BYU FLOW Lab GitHub https://github.com/byuflowlab/CCBlade.jl.git

ϕ, axial induction factor a, tangential induction factor a', and tip speed ratio λ_r at the local blade section.

$$R(\phi) = \frac{\sin(\phi)}{1-a(\phi)} - \frac{\cos(\phi)}{\lambda_r(1-a'(\phi))} = 0 \tag{2.6}$$

From CCBlade we extract axial and tangential induced flow distributions to be able to compute the propeller influence on the wing. We calculate only the propeller wake induced velocity so behind the propellers the freestream velocity is not applied twice to the wing. This BEM formulation uses 2D airfoil data to calculate the induction factors for each annular disk of the propeller (fig. 2.1) including Prandtl hub and tip loss correction factors [28].

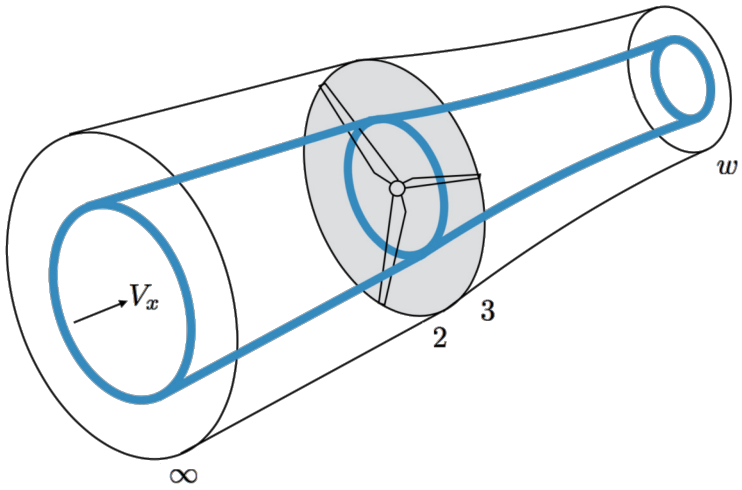

Figure 2.1: The blue streamtube depicts an annular control volume used in blade element momentum theory including the oncoming freestream (V_x) at the upstream plane (∞), the rotor plane (2 and 3), and the far wake (w) with a representation of the wake contraction.

To properly model the induced wake velocity in BEM formulation, the tip loss factors must be included in the output induced velocities. The hub and tip loss equations are reproduced here with the intermediate and final hub loss correction factors f_{hub} and F_{hub} in eqs. (2.7) and (2.8) including the number of blades B, blade radial position r, and blade radius at the hub R_{hub}.

$$f_{hub} = \frac{B}{2}\left(\frac{r-R_{hub}}{R_{hub}\,|\sin(\phi)|}\right) \tag{2.7}$$

$$F_{hub} = \frac{2}{\pi} cos^{-1}(e^{-f}) \tag{2.8}$$

The tip loss equations follow similarly to the hub loss equations in eqs. (2.9) and (2.10), with the total Prandtl loss factor F in eq. (2.11).

$$f_{tip} = \frac{B}{2}\left(\frac{R_{tip} - r}{r|\sin(\phi)|}\right) \tag{2.9}$$

$$F_{tip} = \frac{2}{\pi} cos^{-1}(e^{-f}) \tag{2.10}$$

$$F = F_{hub} F_{tip} \tag{2.11}$$

As shown in eqs. (2.12) and (2.13), the total loss factor is then applied to the axial and tangential induction factors that were solved for in the residual equation. The induction factors are the fractional increase in the inflow velocities (corrected for AOA) in the axial and tangential directions, V_x and V_y, which gives the propeller induced wake velocities in the axial and tangential directions, V_{xw} V_{yw}.

$$V_{xw} = V_x a F \tag{2.12}$$

$$V_{yw} = V_y a' F \tag{2.13}$$

Propeller wakes generally reach their far-field values within approximately one rotor radius [29], and in these conceptual design studies we model the propeller as being removed one radius or more from the wing for the far-field values to be applied on the wing. This removes the need to model slipstream contraction and the associated changes in wing angle of attack and spanwise flow that would otherwise be present with a propeller closer than one radius to the wing. This configuration is similar to tests conducted by Epema [30]. In the far-field, the induced velocities are double what they are at the rotor plane as required by momentum theory. Additionally, as previously shown by Veldhuis and Epema [30, 31] in their experimental results, not all of the

tangentially induced velocity from the propeller is applied normal to the wing chordline. This reduction, or swirl reduction factor (SRF), is approximately 0.5 [31] for a propeller in line with the wing chord.

Calculating the slipstream contraction includes a simple momentum balance between the flow rate at the rotor station and the far wake in the BEM control volume. We model the annular contraction as being fixed at the wake center with the contraction compounding to the edge of the stream tube as done by Veldhuis [31]. Although we include this slipstream contraction, we use the fully developed contraction when passing the propeller wake to the wing, consistent with the propeller being removed at least one radius from the wing. Applying the fully developed wake on the wing has the advantage of removing the need to model changes in the wing angle of attack due to wake contraction. The equation for the annular area contraction including axial induction, C_r, is seen in equation (2.15) with the propeller tip radius R, and distance from the rotor plane in the wake direction x_w. The mean axial induction $\bar{a}$ is used as shown in equation (2.14) with the average induced axial velocity u and the freestream velocity V_x.

$$\bar{a} = mean\left(\frac{u}{V_x}\right) \tag{2.14}$$

$$C_r = \sqrt{\frac{1+\bar{a}}{1+\bar{a}\left(1+\frac{x_w}{\sqrt{R^2+x_w^2}}\right)}} \tag{2.15}$$

2.2.1 Airfoil Pre-computation

To accurately predict the propeller performance with blade element momentum theory, accurate airfoil data is required. To achieve this, we use XFOIL[3,4] to run the Eppler 212 airfoil for 13 Reynolds numbers ranging from 5×10^4 to 1×10^8, five Mach numbers ranging from 0 to 0.8, and 51 angles of attack ranging between negative and positive stall (approximately negative 10° to positive 20°, depending on the Reynolds and Mach number). The E212 airfoil is designed for

[3]pyXLIGHT on MDO Lab Bitbucket https://bitbucket.org/mdolab/pyxlight
[4]Xfoil.jl on BYU FLOW Lab GitHub https://github.com/byuflowlab/Xfoil.jl

the low Reynolds numbers that the propellers in this study operate. The airfoil also has favorable characteristics in terms of a relatively soft stall and high lift to drag ratio which also enables efficient convergence in XFOIL. The wide ranges of operating conditions are used to enable the optimization algorithm to step through the design space with more accurate gradients.

We use Airfoilpreppy[5] [32] to model the stall delay experienced by local sections on rotating blades. This code applies the rotational correction on lift by Du et al. [33] and drag by Eggers et al. [34] as well as extrapolation to high angles of attack by Viterna et al. [35]. In order to validate the lift correction, we model the same experimental data as used by Du et al. in their study for the FFA airfoil of the STORK 5 WPK wind turbine. Using the FAA airfoil geometry and running it in XFOIL, we are able to calculate the 2D sectional lift coefficient. As seen in fig. 2.2, we are able to match the 3D experimental trends much more closely than the 2D data. We find a standard deviation on the error of 0.057 and 0.061 for the lower and upper curves for the corrected data as opposed to 0.10 and 0.53 for the 2D data.

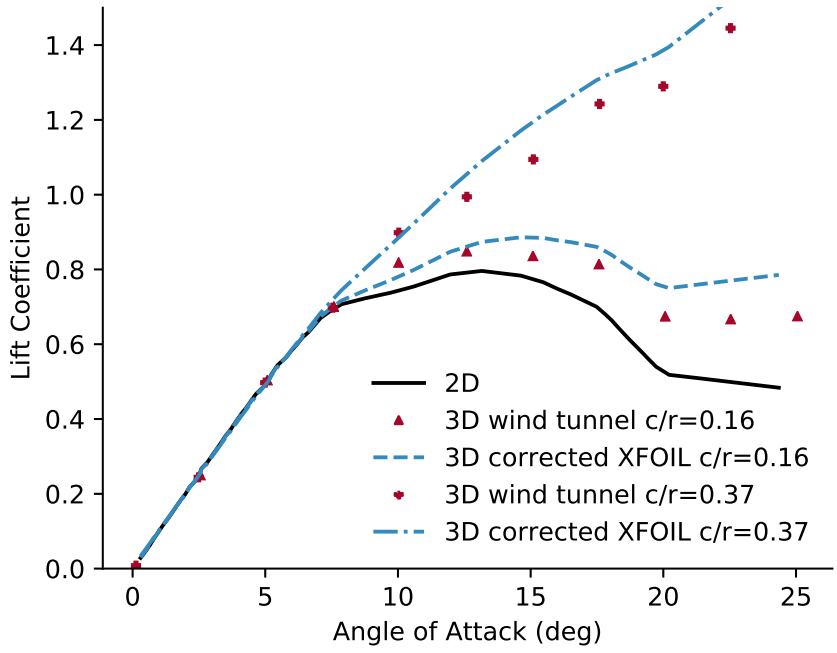

Figure 2.2: Validation of 3D rotational stall correction with experimental data from [33] for two different chord to radius c/r ratios of the FFA airfoil on the STORK 5 WPX wind turbine.

[5] AirfoilPreppy on BYU FLOW Lab GitHub https://github.com/byuflowlab/AirfoilPreppy.git

To verify the extrapolation method used by Viterna et al. we use the E212 airfoil geometry. We run the airfoil in XFOIL for the ranges of Reynolds and Mach numbers previously stated, as well as between negative and positive stall since XFOIL does not converge with large amounts of flow separation past stall. Using the Viterna extrapolation method provided in Airfoilprep.py, the lift and drag are extrapolated to the full range of angles of attack possible as seen in fig. 2.3 with only three Reynolds numbers shown for simplicity. We should note that while the method has not been fully refined for gradient based optimization, which requires smooth and continuous outputs, the areas of discontinuity occur in the negative stall region. The discontinuity is due to there being no smoothing between the XFOIL and extrapolated data in the areas of negative angles of attack. Negative angles of attack are not within the feasible solution space. Nonlinear constraints on the blade local angle of attack can keep the optimization from encountering numerical difficulty as will be discussed in section 4.1.1. To make the 23,400 airfoil data points quickly accessible during optimization, the data for lift, drag, and moment coefficient was splined using four dimensional B-splines[6].

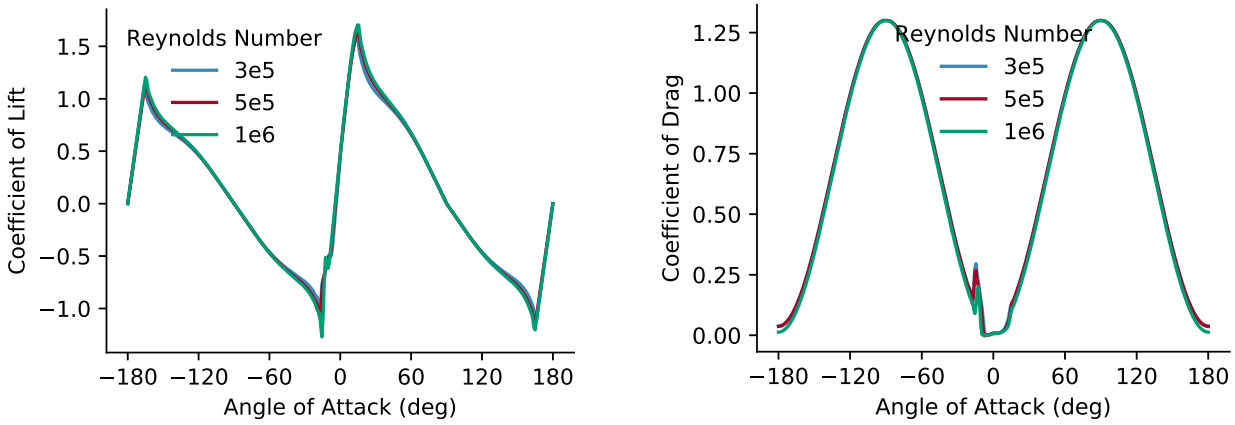

(a) Lift Coefficient

(b) Drag Coefficient

Figure 2.3: Extrapolated E212 airfoil data using the Viterna airfoil extrapolation method. Xfoil data ranges from approx. -10 to 20 degrees AOA with the Viterna airfoil extrapolation method for the remaining range of AOA.

[6]Interpolations.jl on JuliaMath GitHub https://github.com/JuliaMath/Interpolations.jl.git

2.2.2 Propeller Performance Comparison

To validate that the BEM code with XFOIL airfoil data calculation was consistent with Epema's published experimental cases [30], we extracted the propeller geometry from the figures in his report. Using the chord, twist, and airfoil data, we ran XFOIL for the local Reynolds and Mach numbers along the blade. After correcting the airfoil data for rotational stall we use BEM to calculate the thrust and torque at a constant RPM and varying freestream as seen in fig. 2.4. The advance ratio J, or ratio of freestream to rotational rate is defined in eq. (2.16) with the freestream velocity V_∞ in meters per second, the rotation rate n in revolutions per second, and the diameter D in meters.

$$J = \frac{V_\infty}{nD} \tag{2.16}$$

Because we used a different airfoil, the E212 as opposed to the custom airfoils reported, we increased the blade pitch to match the 2D airfoil zero lift angle of attack along the blade. Overall, good agreement in the trends is observed in the propeller efficiency, which is derived from the thrust and torque. A maximum error of 5% can be seen in the normal regions of operation which are the advance ratios below which the steep drop-off occurs. Since the 2D airfoil data includes stall, the effects of stall can be seen on the 3D propeller performance in the very low advance ratios. The more linear regions at the lowest advance ratios are comprised of post-stall angles of attack calculated by the Viterna extrapolation.

2.3 Propeller Noise

In our early versions of this work [22] we used propeller tip speed as a surrogate for noise. We showed that the takeoff performance of a DEP STOL aircraft was much less affected using tip speed constraints, than what we show in this thesis using semi-experimental blade noise. While tip speed captures the magnitude change in noise for a set number of propellers, it is not enough to enable comparison of noise between aircraft designs with different numbers of propellers and the

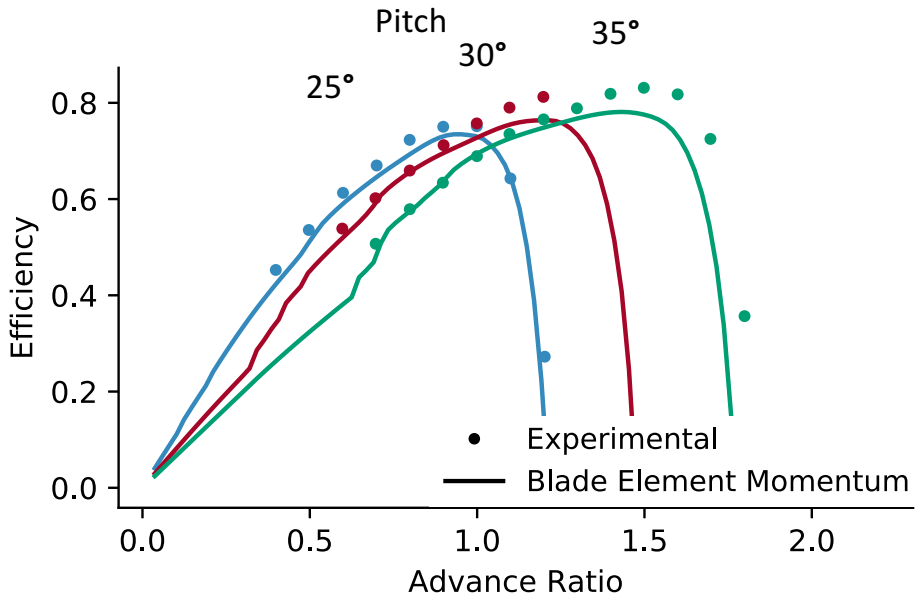

Figure 2.4: Comparison of propeller efficiency with data collected by Epema [30] and the BEM code using XFOIL airfoil data. A maximum error of 5% can be seen in the normal regions of operation which are the advance ratios below which the steep drop off occurs.

associated blade design changes. As will be shown, while the DEP configurations still outperform the traditional configurations, the noise increase scales with more than tip speed alone.

We model propeller noise using code[7] developed and validated by Tingey [36], which uses acoustic modeling techniques by Brooks, Pope, and Marcolini (referred to as the BPM equations) [37, 38]. It is a semi-empirical acoustic model based on experimentation that was conducted using the NACA 0012 airfoil data and includes effects of blade geometry and operation conditions. The types of airfoil noise generation modeled/accounted for include: tip vortex and boundary layer vortex shedding, tip and trailing edge turbulence, and trailing edge bluntness. Additionally, the code uses an A-weighting curve to correct for sound perception and calculates the combined sound pressure level (SPL) of multiple blades at different locations with respect to an observer location. Figure 2.5 shows a graphical representation of the noise profile for an example 8 propeller case in climb at 50 ft with respect to a ground observer. Because this is a comparative conceptual study, we use this semi-empirical noise model as an approximate calculation for the major components of propeller noise. More detailed use of this model would require calibration and validation specific to the application as well as other forms of noise generated by the rest of the aircraft such as from

[7] BPM.jl on BYU FLOW Lab GitHub https://github.com/byuflowlab/BPM.jl.git

the wing, fuselage, electric motors, and motor controllers. However, it captures the main portion of the total noise generation of an electric aircraft enabling us to make a better a comparison between designs with different numbers of propellers, blades, and blade geometry.

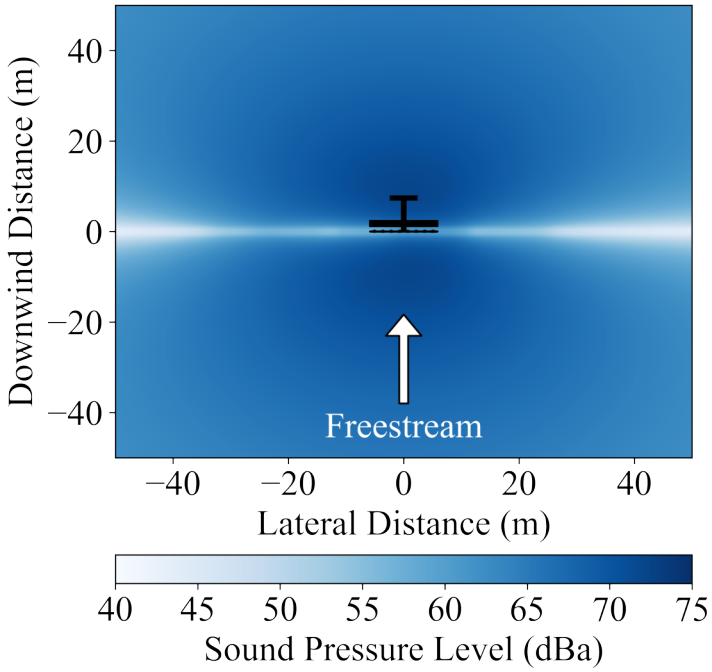

Figure 2.5: Noise profile of example 8 propeller case in climb at 50 ft with respect to a ground observer. (Airframe included for reference.)

To show why using only tip speed is inadequate, we run two test cases to generate contours of the modeled space. First, we generate a noise contour representative of comparing designs with different numbers of propellers based solely on tip speed. Second, we generate a more realistically representative noise contour including the effects of the number of propellers and associated design changes in diameter, chord, and number of blades.

In the first contour, fig. 2.6a, we change only tip speed while holding all else constant and assume that varying number of propellers and the subsequent blade changes are second order and neglected. We use the design and operating conditions, from an example 8 propeller case, typical of the results that will be presented in the final results section. This first noise contour represents the use of tip speed as a surrogate for noise, where regardless of number of propellers, one could

make a direct comparison based only on tip speed. This is incorrect as will be shown in the second case.

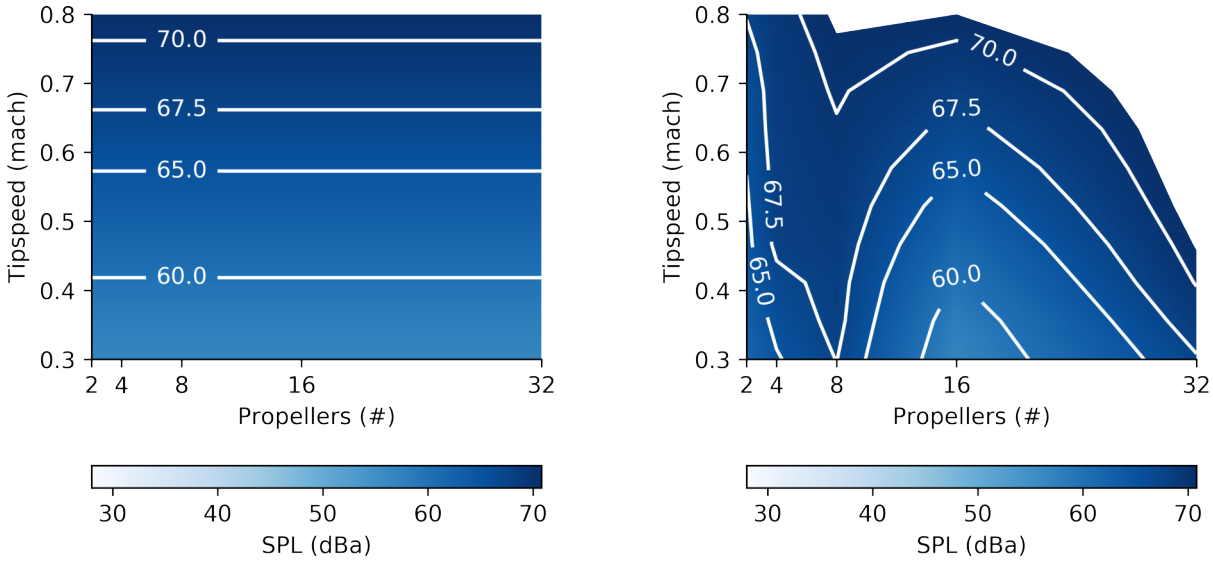

(a) Noise contour representing the assumption of using propeller tip speed as a surrogate for noise. The contour is generated with the results of the 8 propeller, 100 mph cruise, unconstrained noise case assuming varying number of propellers has no effect so there is no change between number of propellers.

(b) Noise contour representative of an example true design space from the results including propeller geometric changes, increasing number of propellers, and increasing number of blades. Clipped at the maximum value of plot (a) for visual emphasis.

Figure 2.6: Propeller noise contours comparing a case with only tip speed changes (representative of using propeller tip speed as a surrogate for noise) and a case representative of propeller design changes as the number of propellers is increased for a DEP STOL system. Tip speed alone is not an adequate measure to compare designs.

In the second case, fig. 2.6b, we run the same sweeps but include propeller design changes. These changes include propeller diameter, number of blades, and blade solidity due to chord and are representative of the final results. When we compare the two plots side by side with the tip speed effects alone on the left and full design changes on the right, it becomes apparent that tip speed alone is not an adequate measure to compare noise between designs with different numbers of propellers. As shown in fig. 2.6b, the more representative case, the 32 propeller case would be required to have a tip speed at Mach 0.45 to achieve a noise level as low as the 16 propeller case at Mach 0.75. Decreasing the SPL to 67.5 dBa makes the difference even more pronounced as seen with the 67.5 dBa contours in both figures. Because of the inadequacy of using tip speed alone to

compare different designs, we have modeled propeller noise with greater fidelity using the BPM equations.

Another metric which further shows the non-uniformity of the noise-design space is the power-to-noise ratio as seen in fig. 2.7 where the power is the power output produced by the electric motors. Here it can be clearly seen that the 8 propeller example is the most noise efficient of the cases shown. The trend tapers off in both directions of varying propeller number with the 32 propeller case being the least noise efficient.

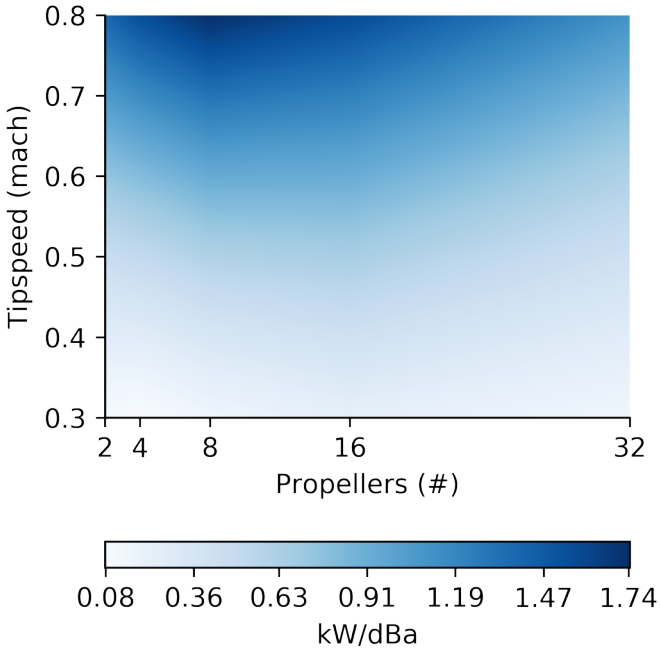

Figure 2.7: Power-to-noise ratio further illustrating the non-uniform tradeoffs between propeller design and noise.

2.4 Composite Structures

Since our objective is to minimize takeoff distance, the propellers will be subject to very high loading to achieve the thrust required on takeoff. To achieve a more realistic total design, we need to include the structural constraints and their effects on the aerodynamic geometry design. These constraints ensure that the blade design and structure meets failure criteria as well as minimum and maximum composite thicknesses. A by-product of this is that the total propeller

mass can be more accurately predicted, which in some cases can be as high as 6% of the allowable propulsion and battery mass.

2.4.1 Propeller Blade Composite Layup

The composite layup for the propellers is defined as a shell with two ply types: unidirectional (or uni) carbon prepreg along the blade span and bidirectional weave (or weave) oriented at 45°. To enable gradient-based optimization for this conceptual study, the plies are modeled with continuous thicknesses. The E212 airfoil normalized geometry can be seen in fig. 2.8 with an example visualization of the composite shell. Shear webs are also built into the code and could be used in future work.

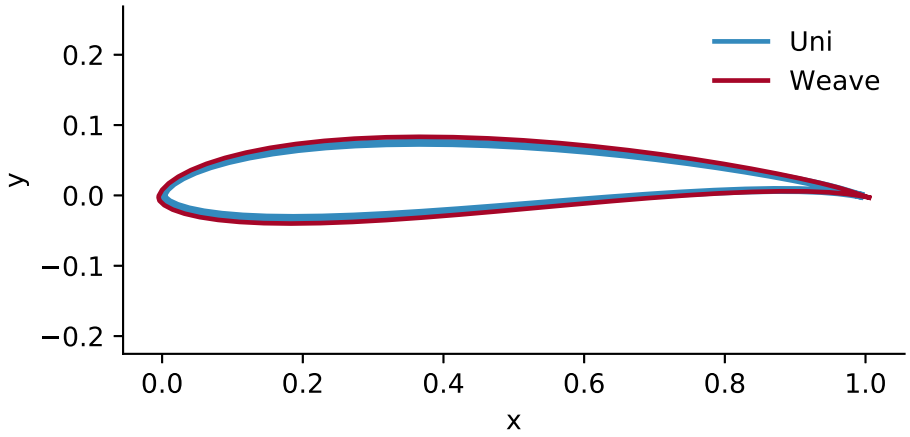

Figure 2.8: E212 Airfoil shell composite layup.

We use PreComp[8,9] to calculate the span-variant sectional properties of the shell, which include mass, stiffnesses, and inertias. From the distributed mass, we calculate each blade mass with trapezoidal integration and scale it according to the number of propellers and blades. PreComp also calculates the structural centers of shear E, mass G, and tension T which are needed to transform the aerodynamic forces from the aerodynamic center R into the structural frame of reference (see fig. 2.9). The relative distances between the structural centers and the aerodynamic center are

[8]PreComp on NREL Information Portal https://nwtc.nrel.gov/PreComp
[9]PreComp.jl on BYU FLOW Lab GitHub https://github.com/byuflowlab/PreComp.jl.git

used to transform the aerodynamic forces at the aerodynamic center, calculated by BEM, into the structural frame of reference.

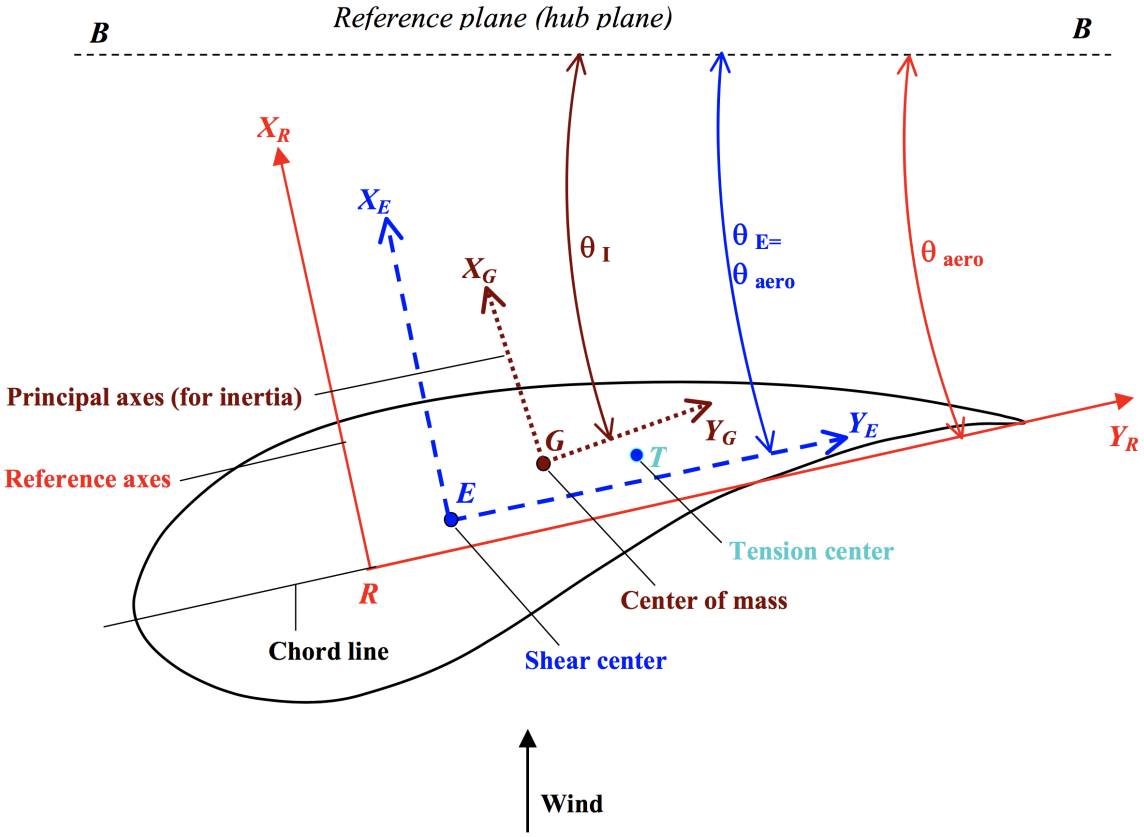

Figure 2.9: Precomp reference axes and centers. (Image reprinted from "Users Guide to PreComp", by G. Bir, 2005, Retrieved from https://nwtc.nrel.gov/PreComp. Copyright 2005 National Renewable Energy Laboratory.

2.4.2 Linear Finite Element Analysis

With the propeller blade distributed stiffnesses calculated from PreComp, we can use linear beam theory [39], a finite element analysis method assuming linear deflections[10,11]. Using the distributed beam properties, we model the blade as a one-dimensional beam fixed at the hub with the propeller aerodynamic loads distributed along the blade. Deflections are calculated by solving the system of equations associated with the assembled beam stiffness matrix, including the fixed

[10]pBEAM on NREL WISDEM GitHub https://github.com/WISDEM/pBEAM.git
[11]BeamFEA.jl on BYU FLOW Lab GitHub https://github.com/byuflowlab/BeamFEA.jl.git

hub zero deflection boundary condition, with respect to the assembled forces and moments matrix. Eigenvalues, or the square of the beam natural frequencies, and eigenvectors, or the beam mode shapes, are calculated similarly with a system of equations but with the assembled stiffness and mass matrices.

Strain calculation is done by integrating the distributed beam stiffness properties between finite sections and multiplying by the respective forces or moments also integrated into the finite sections. Equation (2.17) shows the axial strain ε_{axial} calculation with the axial tension T_x, axial stiffness EA, moment about the y and z axis M_y M_z, flap and lag stiffnesses EI_z EI_y, and y and z distances from the neutral axis (shear center). For this study, strains are calculated for 10 evenly spaced points around the airfoils at 8 sections along the blade using a thin shell approach.

$$\varepsilon_{axial} = \frac{T_x}{EA} + \frac{M_z}{EI_z}y - \frac{M_y}{EI_y}z \tag{2.17}$$

2.4.3 Composite Frame of Reference Stress

To calculate stresses in the composite frame and in turn first ply failure, we use a thin shell calculation with the composite centerline strain for all layers. Calculating composite stress in the composite frame of reference is a multi-step process including calculating the shear strain and laminate stress in the beam frame of reference, then transforming the stress into the ply frame of reference [40]. The shear strain in the beam frame of reference γ_{12} is shown in eq. (2.18) with the shear stress τ, material stiffness matrix in the beam frame of reference $\bar{Q}$, and principle axes strain ε.

$$\gamma_{12} = \frac{\tau}{\bar{Q}_{3,3}} - \frac{\bar{Q}_{1,3}}{\bar{Q}_{3,3}}\varepsilon \tag{2.18}$$

The stress in the beam frame of reference is then calculated as shown in eq. (2.19) using the material stiffness and strains. The stress in the composite frame of reference σ_{ply}, including the ply angle θ, is transformed from the beam stress using the transformation matrix in eq. (2.20).

$$\left[\sigma_1, \sigma_2, \tau_{12}\right] = \bar{Q}\left[\varepsilon, 0, \gamma_{12}\right] \tag{2.19}$$

$$\sigma_{ply} = \left[\sigma_1, \sigma_2, \tau 12\right] \begin{bmatrix} \cos\theta^2 & \sin\theta^2 & 2\sin\theta\cos\theta \\ \cos\theta^2 & \cos\theta^2 & -2\sin\theta\cos\theta \\ -\sin\theta\cos\theta & \sin\theta\cos\theta & \cos\theta^2\sin\theta^2 \end{bmatrix} \tag{2.20}$$

2.4.4 Material Properties

For reference, the composite material properties used are included in table 2.1. The materials included are the carbon fiber reinforced plastic (CRFP) unidirectional (uni) and weave used in the results of this study, as well as the materials used in the validation case presented in section 2.4.6. The units and description of the properties used are as follows: first axis modulus of elasticity e_1 (Pa), second axis of elasticity e_2 (Pa), shear modulus g_{12} (Pa), Poisson's ratio ν,

Table 2.1: Composite Material Properties

Name	e_1	e_2	g_{12}	ν	ρ	x_t	y_t	x_c	y_c	s	t
Uni	$1.75e^{11}$	$0.8e^{10}$	$5.0e^{9}$	0.3	1600.0	$8.060e^{8}$	$6.719e^{8}$	$2.962e^{7}$	$1.667e^{8}$	$5.357e^{7}$	0.152
Weave	$8.5e^{10}$	$8.5e^{10}$	$5.0e^{9}$	0.1	1600.0	$2.821e^{8}$	$1.186e^{8}$	$2.592e^{8}$	$1.250e^{8}$	$3.125e^{7}$	0.218
E-LT	$4.18e^{10}$	$1.4e^{10}$	$2.63e^{9}$	0.28	1920.0	$9.72e^{8}$	N/A	$7.02e^{8}$	N/A	N/A	0.47
Carbon	$1.15e^{11}$	$8.39e^{9}$	$5.99e^{9}$	0.27	1220.0	$1.546e^{9}$	N/A	$1.047e^{9}$	N/A	N/A	0.47
Gelcoat	$3.44e^{9}$	$3.44e^{9}$	$1.38e^{9}$	0.3	1235.0	N/A	N/A	N/A	N/A	N/A	0.05
Triax	$2.77e^{10}$	$1.37e^{10}$	$7.2e^{9}$	0.39	1850.0	$7.0e^{8}$	$7.0e^{8}$	N/A	N/A	N/A	0.94
Saertex	$1.36e^{10}$	$1.33e^{10}$	$1.18e^{10}$	0.49	1780.0	$1.44e^{8}$	$1.44e^{8}$	$2.13e^{8}$	$2.13e^{8}$	N/A	1.0
Foam	$2.56e^{8}$	$2.56e^{8}$	$2.2e^{7}$	0.3	200.0	N/A	N/A	N/A	N/A	N/A	1.0

density ρ (kg/m^3), first axis failure strength in tension x_t (MPa), second axis failure strength in tension y_t (MPa), first axis failure strength in compression x_c (MPa), second axis failure strength in compression y_c (MPa), shear failure strength s (MPa), single ply thickness t (mm).

2.4.5 Material Failure

We use a relatively common method [41, 42], the Tsai-Wu failure criteria [43], to predict first ply laminate failure. This method is a formulation of the general quadratic failure criterion proposed by Gol'denblat et al. [44], specialized for orthotropic classical laminate theory. Tsai-Wu failure theory uses the material strengths and laminate stress in the two principle axes, as well as the shear strength and stress with the two formula eqs. (2.21) and (2.23) that comprise the constraint used during the optimization. This constraint, C_{lam} is satisfied when the sum of a and b are less than 1.0. Constraint values above 1.0 indicate composite failure. First ply composite failure is determined by calculating the failure criteria of all composite layers; the laminate is termed to have failed if any ply fails.

$$a = \frac{\sigma_1^2}{x_t x_c} + \frac{\sigma_2^2}{y_t y_c} - \sqrt{\frac{1}{x_t x_c}\frac{1}{y_t y_c}}\sigma_1\sigma_2 + \frac{\tau_{12}^2}{s^2} \tag{2.21}$$

$$b = \left(\frac{1}{x_t} - \frac{1}{x_c}\right)\sigma_1 + \left(\frac{1}{y_t} - \frac{1}{y_c}\right)\sigma_2 \tag{2.22}$$

$$C_{lam} = (a+b) \tag{2.23}$$

Prior to applying the Tsai-Wu failure criteria, we apply safety factors, material scatter knockdown factors, and barely visible impact damage (BVID) knockdown factors. The material scatter knockdown factors are calculated for the carbon fiber uni and weave based on A-basis values from Tomblin et al. [45, 46]. They are shown in table 2.2 for reference and have already been applied to the uni and weave in table 2.1. The BVID knockdown factor was chosen to be 0.65 [40] and the safety factor to be 1.5.

Table 2.2: Material Scatter Knockdown Factors

Material	k_1^+	k_1^-	k_2^+	k_1^-	k_{12}
T300/934 tape	0.625	0.762	0.803	1.0	0.920
T300/934 fabric	0.764	0.776	0.719	0.859	1.0

To predict buckling, we assume long, simply-supported plates and calculate buckling strain with respect to the composite stiffness as described by Johnson et al [47]. The critical buckling stress N_{cr} is comprised of a formulation of the classical laminate theory D-stiffness matrix D and simply supported span b as shown in eq. (2.24). For structures including shear web(s), the simply supported span lengths would become the respective distances between support points such as the trailing edge, shear web(s), and leading edge. This critical buckling stress is transformed into the beam frame of reference strain as shown in eq. (2.25) using the composite laminate theory A stiffness matrix A.

$$N_{cr} = 2\left(\frac{\pi}{b}\right)^2 \sqrt{D_{11}D_{12}} + D_{12} + 2D_{22} \tag{2.24}$$

$$\varepsilon_b = \frac{N_{cr}}{A_{11} - \frac{A_{12}^2}{A_{22}}} \tag{2.25}$$

2.4.6 Aerostructural Verification

To verify the aerostructural aspect of the code we used results from a wind turbine study that also used blade element momentum and PreComp, but with the higher fidelity ANSYS finite element analysis package for structural analysis [48]. Wind turbine analysis is identical to propeller analysis [49], but with different boundary conditions in the BEM; an expanded wake with half the induced velocity in the far field (momentum is removed from the flow for a wind turbine as opposed to being increased). We modeled the Sandia National Laboratories (SNL) 61.5 meter wind turbine blade with the reported airfoil properties, geometry, composite material properties, and layup schedule at each of the blade sections including the spar and shear web. A sample section of the wind turbine is shown in fig. 2.10, where, starting from the trailing edge and moving right, there is the trailing edge (te), reinforced trailing edge thicknesses (te-reinf), trailing edge panel (te-panel), first shear web (web 1), reinforced spar cap (cap), second shear web (web 2), leading edge panel (le-panel), and leading edge (le). The composite thicknesses were modeled as being the same for both upper and lower sections of the blade.

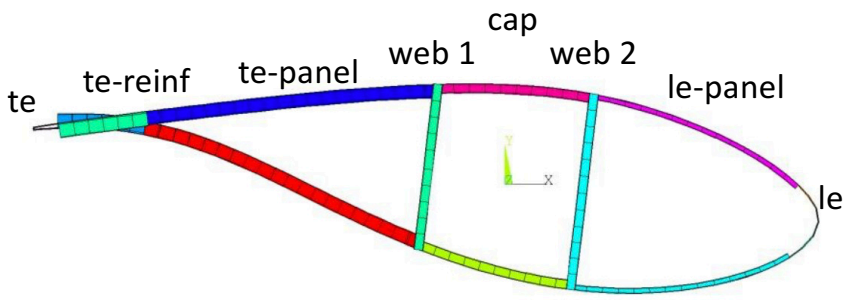

Figure 2.10: Composite sections of the SNL 61.5 m wind turbine for airfoil geometry at 30.0 m span. From left to right: trailing edge (te), reinforced trailing edge thicknesses (te-reinf), trailing edge panel (te-panel), first shear web (web 1), reinforced spar cap (cap), second shear web (web 2), leading edge panel (le-panel), and leading edge (le). (Image reprinted from "Definition of a 5mw/de.5m wind turbine blade reference model", by B. Resor, 2013, Retrieved from https://prod.sandia.gov/techlib-noauth/access-control.cgi/2013/132569.pdf. Unlimited Release Sandia National Laboratories.)

Figure 2.11 shows the individual layer thicknesses and ply ID numbers for the composite layer types used. The dots in the figure represent the originally reported values and the lines represent our piecewise linearly interpolated values. Table 2.1 gives the material properties for each of the layers. There is some deviation at the radial blade locations where the original data was reported due to the numerical splining package used, but which does not significantly affect the distributed properties as will be discussed.

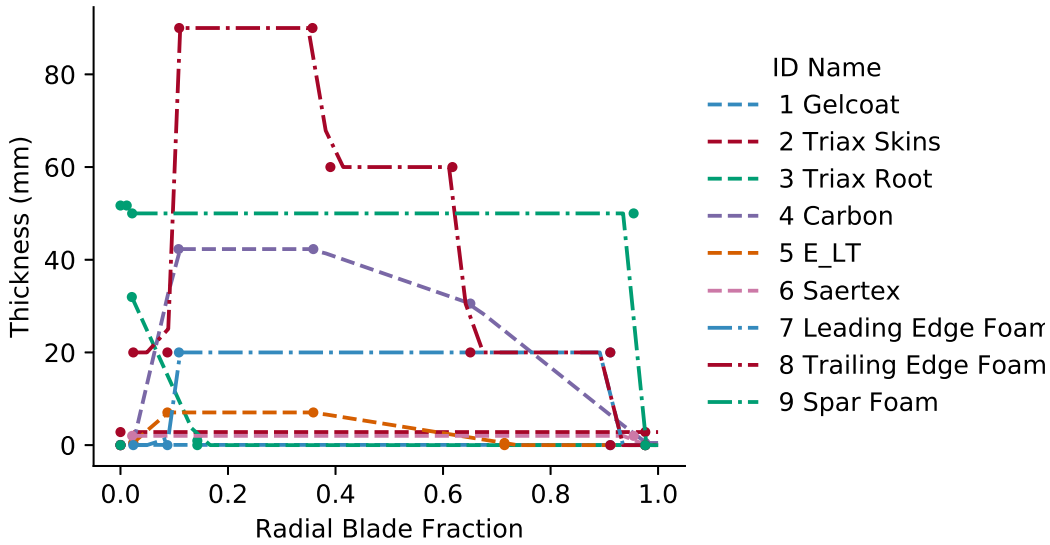

Figure 2.11: Composite thicknesses for the SNL 61.5 meter wind turbine blade. Dots are data as extracted from Resor's report [48] and lines correspond to the splined values used.

Table 2.3: Blade Skin Stacking Sequence.

Blade Span (m)	te	te-reinf	te-panel	cap	le-panel	le	web 1	web 2
0	1,2,3,2	1,2,3,2	1,2,3,2	1,2,3,2	1,2,3,2	1,2,3,2	none	none
1.3667	1,2,3,2	1,2,3,2	1,2,3,2	1,2,3,2	1,2,3,2	1,2,3,2	6,9,6	6,9,6
1.5	1,2,3,2	1,2,3,5,8,2	1,2,3,8,2	1,2,3,4,2	1,2,3,7,2	1,2,3,2	6,9,6	6,9,6
6.8333	1,2,3,2	1,2,3,5,8,2	1,2,3,8,2	1,2,3,4,2	1,2,3,7,2	1,2,3,2	6,9,6	6,9,6
9	1,2,2	1,2,5,8,2	1,2,8,2	1,2,4,2	1,2,7,2	1,2,2	6,9,6	6,9,6
43.05	1,2,2	1,2,5,8,2	1,2,8,2	1,2,4,2	1,2,7,2	1,2,2	6,9,6	6,9,6
45	1,2,2	none	1,2,8,2	1,2,4,2	1,2,7,2	1,2,2	6,9,6	6,9,6
61.5	1,2,2	none	1,2,2	1,2,2	1,2,2	1,2,2	6,9,6	6,9,6

The final part in describing the composite layup is shown in table 2.3 where the material ID numbers can be found in fig. 2.11. The stacking sequence starts at the top of the laminate, proceeding downward. While the stacking sequences in the table show the termination of certain layers at varying sections along the blade, a simplification can be made in the code when modeling the stacking sequences. It is numerically equivalent and less complex to include all layers at every blade location but assign zero thicknesses a layer if it is not used.

With the blade composites and geometry fully defined, we use PreComp to evaluate the distributed structural properties. An example showing our results at this step is shown in fig. 2.12 for the mass and flap-wise bending stiffness distributions compared to the SNL values and also values from a study conduced at the National Renewable Energy Lab (NREL) [50].

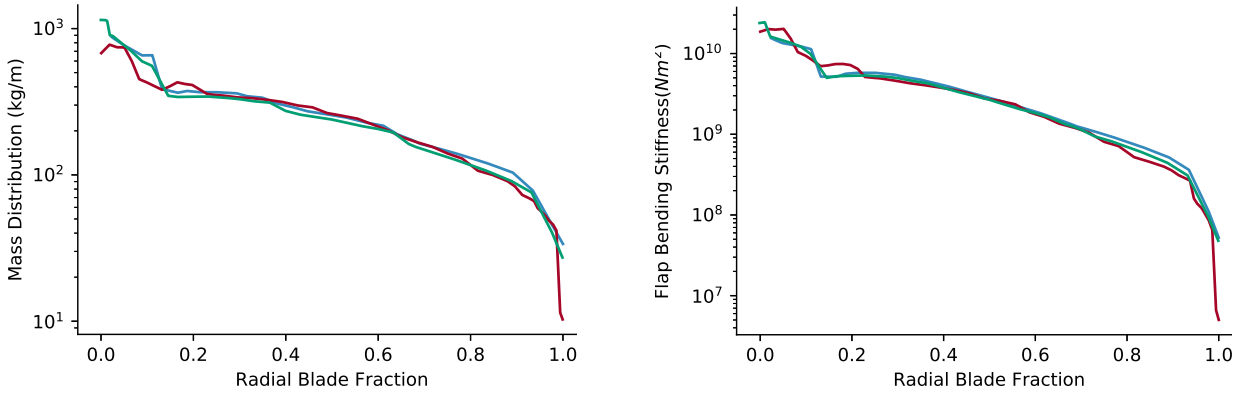

(a) Mass Distribution

(b)

Figure 2.12: Comparison of mass distribution and flap-wise bending stiffness for the SNL 61.5 m wind turbine. Present study in blue, SNL in green, and NREL in red.

Running the blade at the reported operating conditions of maximum efficiency (power coefficient) at the rated wind speed, we found our strain to match the reported strain within 5%. A graphical representation of our model of the blade can be seen in fig. 2.13 including the strain contour for the case. Composite stress and buckling stress was not reported in the SNL report, but both were within the safety factors required.

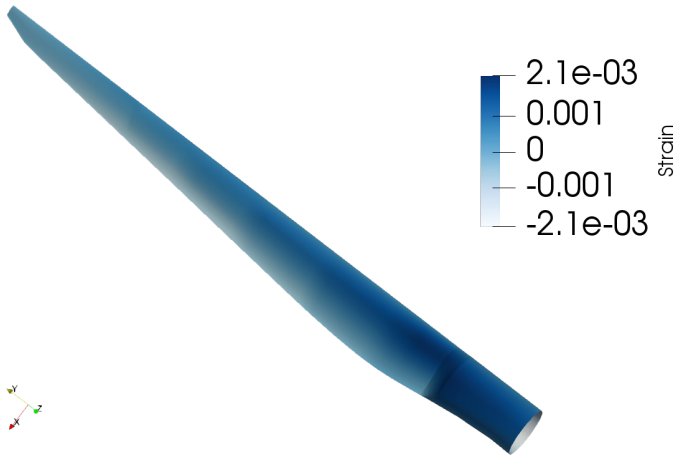

Figure 2.13: Graphical strain contour of the Sandia National Labratories 61.5 wind turbine created using our aerostructural framework. Reported strain matches within 5% while composite stresses and buckling were within the reported safety margins.

2.5 Waked Wing Modeling

The vortex lattice method (VLM) is a discretized lifting line theory that calculates the inviscid lift and lift-induced drag for non-uniform freestream and geometry [51]. Typically the method is implemented with a uniform freestream that is applied independently at each vortex boundary condition. In order to account for the propeller on wing effects, we have included the propeller axial and tangential velocity distributions in the boundary condition similar to that done by Veldhuis [31]. Equation (2.26) gives the typical normal velocity boundary condition due to freestream $V_{n\infty}$ applied to the VLM including angle of attack α, local twist angle θ, wing dihedral Γ_w, and freestream velocity V_∞.

$$V_{n\infty} = V_\infty \cos(\alpha)\sin(\theta) \; + \; V_\infty \cos(\theta)\sin(\Gamma_w) \; + \; V_\infty \sin(\alpha)\cos(\theta)\cos(\Gamma_w) \tag{2.26}$$

However, since we are applying the propeller induced wake velocities as well, we calculate the additional normal velocity boundary condition V_{nw} as seen in eq. (2.27) with induced wake velocities in the x or axial direction V_{xw}, as well as velocities in the y V_{yw}, and z V_{yw} directions. It is important to note that by using the propeller induced wake velocities, we are not double counting the freestream velocity on the wing in the waked regions. With the propeller in line with the wing and the hub at the chord line, the wake y velocity is zero and all of the swirl velocity is contained in the z direction (up relative to a flat wing). Propeller induced velocities are zero between propeller tips. The total normal boundary condition V_n shown in eq. (2.28) is the sum of the two normal velocities. This VLM[12] was developed and validated previously for formation flight studies, for which similar wake-wing interactions exist [52].

$$V_{nw} = V_{xw}\sin(\theta) \; - \; V_{yw}\cos(\theta)\sin(\Gamma_w) \; + \; V_{zw}\cos(\theta)\cos(\Gamma_w) \tag{2.27}$$

$$V_n = -(V_{n\infty} + V_{nw}) \tag{2.28}$$

Specifically regarding the tangential, or swirl velocity, induced by the propeller, it is important to note that not all of this velocity is applied to the boundary condition in the vortex lattice method [53]. Neglecting a correction on the swirl velocity over-predicts its effect on the wing lift distribution as previously noted by Hunsaker [54] with the local lift coefficient being over-predicted by as much as 6x. Additionally, the optimal blown lift distribution is non-elliptical [55], which makes the propeller on wing interaction critical for design. Momentum from the propeller that is induced downward is accounted for in the induced drag. An extra propeller swirl loss D_{swirl} from the propeller tangential velocity on the Trefftz plane is also included as described by Veldhius [31] and shown in eq. (2.29) with the surface of the propeller wake plane s_p parallel to the rotor plane.

$$D_{swirl} = \iint_{s_p} V_{yw}^2 + V_{zw}^2 \, \mathrm{d}s \tag{2.29}$$

[12]BYU FLOW Lab GitHub VLM.jl https://github.com/byuflowlab/VLM.jl.git

The current models are simplified from Veldhuis' work and do not include several extra effects. These include first, the propeller slipstream will not be above or below the wing so non-symmetric wake modeling is not necessary. Second, the propellers will be removed at least one propeller radius from the wing so that wing on propeller interactions and slipstream contraction are second order. However, we do include viscous drag and critical section stall theory. Viscous, or parasitic drag, is calculated using strip theory with XFOIL for a given angle of attack (including wing and propeller induction effects), Mach number, and Reynolds number. To account for the wing viscous drag in the propeller wake, we assume fully turbulent transition and run XFOIL with a forced transition boundary condition at the airfoil leading edge. To speed up the optimization process, we precompute these values and use a three dimensional cubic B-spline interpolation method which returns continuously differentiable outputs. Critical section stall theory is simply that stall is predicted when the local lift coefficient cl meets a specified maximum local lift coefficient cl_{max} anywhere along the wing. To prevent the wings from stalling before the inboard sections, we impose a 20% reduction in the allowable local lift coefficient on the last 5% of the wing span. The allowable local lift coefficient, normalized by the local velocity is 2.4 for takeoff and 1.2 during cruise. The local lift coefficient stall constraint of 2.4 is a surrogate for extended flaps with a zero lift angle of attack at -14 deg for a single slotted flap at 30 deg deflection [56]. The local lift coefficient of 2.4 is also a 10% margin below the maximum local lift coefficient of the flap configuration chosen.

2.5.1 Prop on Wing Smoothing

While vortex lattice methods can be evaluated rapidly, their discrete panels can create difficulties with gradient-based optimization. This problem arises for this study because we are interested in exploring different propeller sizes as a design variable. As the propeller diameter changes, the propeller wake blankets a different number of VLM panels. Specifically, as the wake moves over a new control point, the predicted forces and moments change in a discontinuous manner.

To overcome the discontinuities, our methodology has two parts. First, we ensure that the center of the propeller wake is centered on a wing control point. Because the position and number

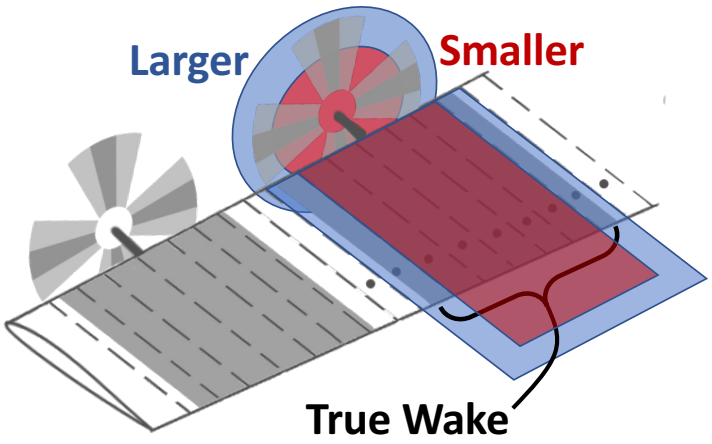

Figure 2.14: A representation of the strategy used to evaluate changing rotor diameters. Rotor wake is oversized to fit in the blue, then undersized to fit in the red, then the resulting analyses are linearly interpolated to the actual rotor wake (shaded grey). Viscous drag is also included in the interpolation allowing for partial waking of the VLM panels for the viscous model as well

of propellers are fixed during the optimization, these locations can be precomputed. Also, since the propeller and control point locations are non-dimensionalized based on the wingspan, the span can be added as a design variable for constant propeller relative locations and number of control points. Second, for each wake diameter we find the two nearest far field diameters, one smaller and one larger, that exactly cover full panels (see fig. 2.14). To apply the stretched wake to the control points, we use linear interpolation and scale the wake span-wise location based on the new diameter for each case.

We evaluate the VLM at both the smaller diameter and larger diameter conditions, then linearly interpolate the VLM outputs using the wake diameter (this is not the same as the rotor diameter because of wake contraction). The linear interpolation is applied to scalar values as well as arrays, such as the wing distributed lift and drag. This is particularly useful since the viscous drag can also be included in the interpolation allowing for partial waking of the VLM panels for the viscous model as well. The linear interpolation is done by the simple interpolation fraction calculation seen in eq. (2.30) with the interpolation fraction f_i, the effective rotor diameter D_{eff}, the smaller rotor diameter D_s and the larger rotor diameter D_l. The interpolation fraction is applied to the scalar or array values of interest as shown in eq. (2.31) with the desired value(s) x, the

value(s) from the smaller rotor diameter analysis x_s, and the value(s) from the larger rotor diameter analysis x_l.

$$f_i = \frac{D_{eff} - D_s}{D_l - D_s} \tag{2.30}$$

$$x = x_s + f_i * (x_l - x_s) \tag{2.31}$$

A comparison of the old method and new linear interpolation method is shown in fig. 2.15 with the wing lift coefficient C_L, and wing induced drag coefficient C_{Di}. The original function contains many artificial local minima, while this modified approach produces a differentiable output. While this modification does require twice the number of function calls to the VLM, it allows for rotor diameter to be directly included in the optimization. Not including the rotor diameter in the optimization increases the complexity of the problem by making the problem combinatorial, or we would also have to perform a variable sweep of the propeller diameter for each of the numbers of propellers tested.

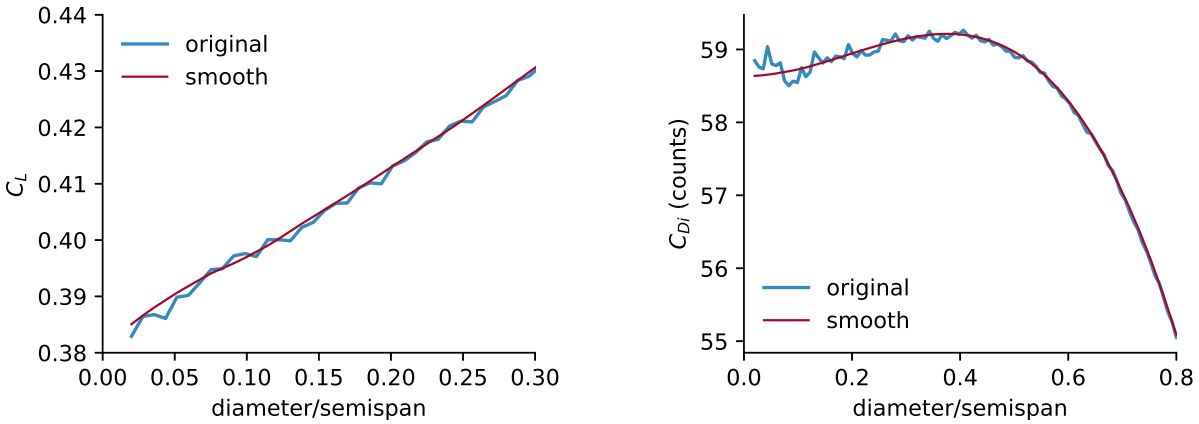

(a) lift coefficient

(b) induced drag coefficient

Figure 2.15: A comparison between the original VLM output and our modified approach with changing rotor diameter. As the propeller diameter changes, the propeller wake discretely intersects with wing control points creating noisy output. Our modified approach allows for smooth variations with changing propeller diameter. The lift coefficient is shown on a smaller x-axis range because the oscillations are smaller and are harder to see when zoomed out.

2.5.2 Propeller on Wing Validation

We examined two separate validation cases for the propeller on wing interaction. The first case is from wind tunnel data of a single propeller on a straight untwisted wing by Veldhuis [31,55]. Data is available at two angles of attack: 0°, and 4°. Figure 2.16a shows a comparison between the experimental lift coefficient and that predicted by our methodology for both angles of attack. Agreement is observed in fig. 2.16a with a standard deviation on the error of 0.009 and 0.015 for the upper and lower curves respectively with error being greatest at the propeller slipstream boundary.

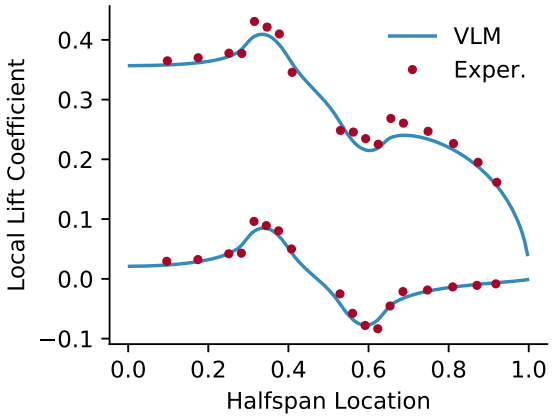

(a) Lift coefficient distribution from our BEM/VLM compared to Veldhuis experimental wind tunnel data at two angles of attack.

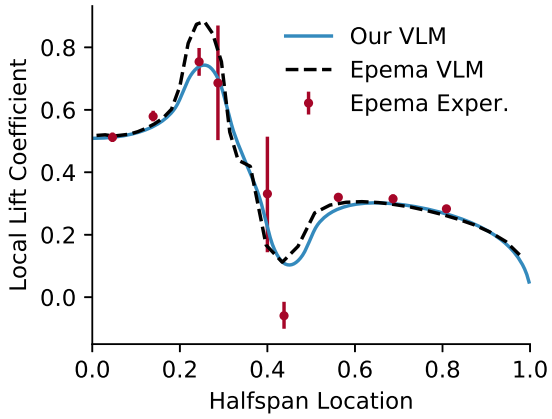

(b) Lift distribution from our BEM/VLM compared to Epema VLM and experimental data. Error bars show one standard deviation.

Figure 2.16: Two validation cases for propeller on wing interaction using two different geometries.

The second set of experiments comes from a separate wind tunnel experiment by Epema [30], using a larger propeller and a tapered wing. We compare the results for the lift distribution for our VLM, the VLM developed by Epema in that same study, and the wind tunnel data. Reported error bars in the wind tunnel data are included in fig. 2.16b and are due to the dynamic nature of the propeller helical vorticies [29]. The two VLMs tend to follow the experimental trends except where the propeller swirl velocity induces wing upwash in the half-span regions between 0.2 and

0.3. In this region our VLM more closely matches the experimental data and overall has a standard deviation of error of 0.07 with respect to the mean experimental values.

2.6 Electric Components Modeling

Based on the results of this study, the motor and motor controller can fill as much as 88% of the total available battery and propulsion mass. Additionally, a less efficient motor may require more current, and in turn a larger mass, to output the same amount of power as a more efficient motor. Therefore, with this type of aircraft problem where the mass has a significant coupled effect due to lift induced drag, mass modeling is a critical part of this conceptual design.

2.6.1 Electric Motor

For calculating motor efficiency and power, we use a fundamental first order motor model [57]. This model treats the motor as a simple resistive circuit with an additional internal voltage drop modeled as a voltage sink as seen in fig. 2.17. The parameters used in the model include the rotational speed constant K_v, the no-load current I_0, the no-load resistance R_0, torque Q_m, internal voltage drop V_m, total voltage drop V, current i, and rotational speed Ω_m. This model assumes no losses due to increased resistance from heating. A second order model that does include these effects is also available by the same author [58], but requires heat transfer modeling.

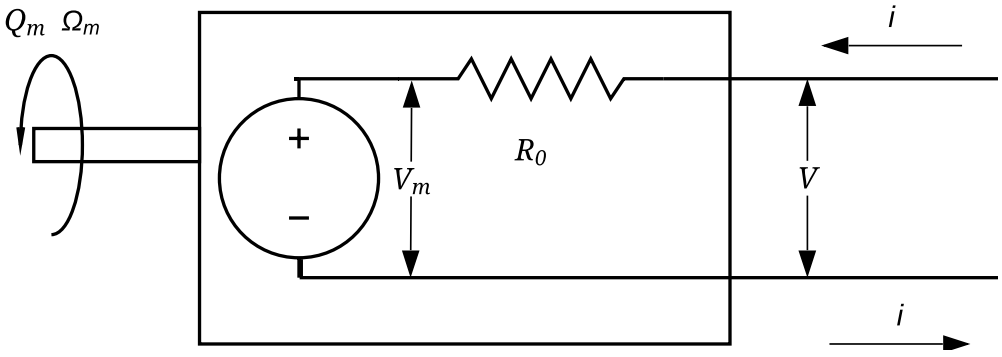

Figure 2.17: Electric motor equivalent circuit.

The motor efficiency as calculated in eq. (2.35) follows the progression: In eq. (2.32), the motor current is calculated based on the no-load current and the torque multiplied by the rotational speed constant. This model assumes the torque constant equals the rotational speed constant due to the limiting zero losses case and energy conservation as shown by Drela [57]. The motor internal voltage drop is calculated from the rotation rate and rotational speed constant in eq. (2.33), which is then used in conjunction with the current, no load resistance, and Ohm's Law to calculate the total motor voltage drop in eq. (2.34). Finally, the formulation for the motor efficiency based on the required rotation rate and torque as well as motor parameters is shown in eq. (2.35). Comparing the first order model to the Maxon 305013 Brushless Motor[13] data, we found the efficiency, current, and required voltage to all be within 1.5% for the nominal RPM and torque.

$$i = I_0 + KvQ \tag{2.32}$$

$$V_m = \frac{\Omega}{Kv} \tag{2.33}$$

$$V = V_m + R_0 i \tag{2.34}$$

$$\eta_m = \left(1 - \frac{I_0 R_0}{V - \frac{\Omega}{Kv}}\right)\left(\frac{\Omega}{VKv}\right) \tag{2.35}$$

In order to model the motor mass, we created a linear fit to the motor data from the Astroflight[14] line of motors. Astroflight motors were chosen due to the availability of data and the favorable range of both power and Kv. We found a linear relationship between the mass and the motor peak current divided by the motor K_v parameter (fig. 2.18a). This reduces to electric-power/RPM where this power is the motor electrical power under load. If we assume no efficiency losses, this term further reduces to torque. The line fit in eq. (2.36) shows the trend of the best motors and is used in estimating the motor mass and has an R^2 value of 0.94. The motors included in this empirically-based model ranged from 1.5 kW to 15 kW and K_v from 32 to 1355.

[13] Maxon Motors Online Catalog http://www.maxonmotorusa.com, accessed 7/12/18

[14] Astroflight Motors astroflight.com, accessed 7/11/18

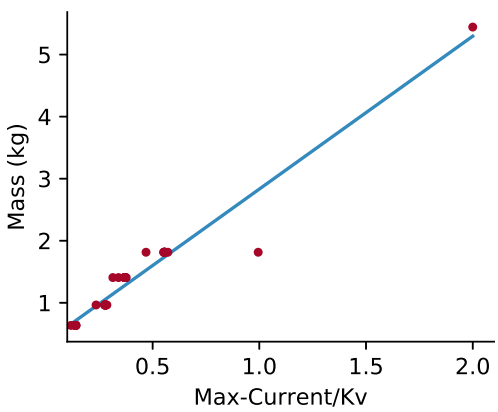

(a) Motor mass fit using Astroflight motor data in blue with data in red. The equation for the linear fit is shown in eq. (2.36).

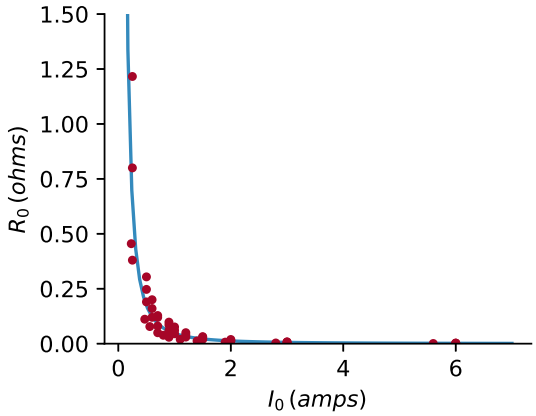

(b) Astroflight motor fit for I_0 and R_0 in blue and data in red, equation shown in eq. (2.37).

Figure 2.18: Data fits based on Astroflight motor data.

$$m_{motor} = 2.464\,\frac{I_m}{K_v} + 0.368 \tag{2.36}$$

To accurately model motor performance in addition to mass, we investigated the relationship between all of the motor parameters. We found that there were no interdependencies other than those between first the mass, motor peak current, and K_v, and second between the no-load resistance and no-load current. The trend for the latter can be seen in fig. 2.18b and the accompanying fit in eq. (2.37) with an R^2 value of 0.93.

$$R_0 = 0.0467(I_0)^{-1.892} \tag{2.37}$$

2.6.2 Linearized Battery and Motor Controller Masses

Due to the scope and nature of this comparative conceptual design study, we used a simplified approach to model the motor controller and battery masses. The motor controller model for mass was assumed to be linear based on the specific power of 22,059 W/kg taken from the

Astroflight high voltage motor controller.[15] Efficiency of the motor controller was assumed to be a constant 97%. The battery was modeled with a specific energy parameter of 300 Wh/kg, representative of a mid-life, currently available Li-S battery [59]. We have not included the second order effects of current draw or temperature on cell voltage or efficiency. These second order effects, if included, would effectively decrease the specific energy of the battery similarly to what we have already done to represent a mid-life battery cell.

[15] Astroflight Motor Controller astroflight.com/esc-2413, accessed 12/9/17

CHAPTER 3. AIRCRAFT TAKEOFF PERFORMANCE

While it would be more ideal to model the full balanced field length, as will be discussed in the results section, the time to liftoff is on the order of seconds. This means that the pilot reaction time of approximately 1 second [60] could make an aborted takeoff infeasible before liftoff. A revised balanced field length calculation for this type of aircraft including concepts discussed by Patterson [18] may be in order. Due to this uncertainty in the proper balanced field length calculation, we focused on the minimum conceptual takeoff distance including ground roll, transition, and climb. For simplicity and as a conservative factor we did not include the beneficial effects of ground effect in our takeoff distance calculations.

In our final results for this type of STOL aircraft, we found ground roll distance alone accounts for less than than 20% of the total distance to clear a 50 ft obstacle. Additionally, the transition distance from liftoff to steady climb must be accounted for due to the large flight path angles encountered and can exceed 30% of the total takeoff distance. A graphical representation of the three parts of takeoff can be seen in fig. 3.1, where the figure is scaled to represent an example 8 propeller case typical of the results. In light of these requirements, we review the aircraft acceleration for constant power, transition, and steady climb, all adapted for high angles of attack. We also review the aircraft range calculation.

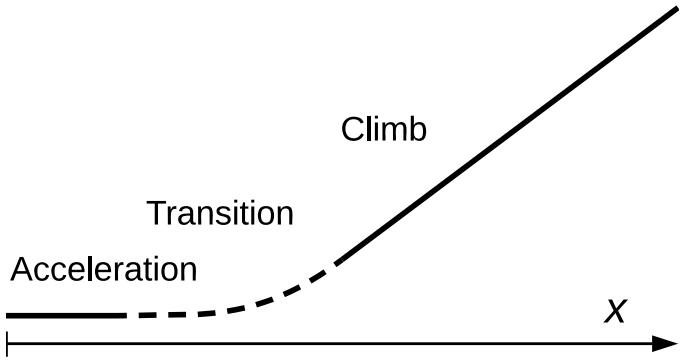

Figure 3.1: Example takeoff profile scaled to represent a sample 8 propeller case. Takeoff transition becomes significant when the flight path angle is greater than a few degrees.

3.1 Ground Roll Distance / Acceleration

To model the ground roll, or acceleration distance, we use an approach similar to Anderson's [61] constant thrust approach. His approach assumes the aircraft starts from rest and is accelerated to the takeoff speed with a constant thrust and mass, and an averaged drag. While turbine engine based propulsion is assumed to have a constant thrust during takeoff, electric propulsion is assumed to have a constant power during takeoff. Because of this, a slight variation in Anderson's takeoff rolling distance equation is required. Beginning with the same assumptions (constant mass, acceleration from rest, and average drag) as in his takeoff performance equation, we modify the derivation to assume a constant power during takeoff resulting in the following integration for takeoff roll distance where s_{GR} is the ground roll distance, m is the total mass, V_∞ is the freestream velocity at liftoff, $P_{net,out}$ is the net power output (total power less power due to average drag). (See eq. (3.1))

$$s_{GR} = \frac{mV_\infty^3}{3P_{net,out}} \tag{3.1}$$

For battery sizing, we also use the ground roll distance time at constant power as seen in eq. (3.2).

$$t_{GR} = \frac{mV_\infty^2}{2P_{net,out}} \tag{3.2}$$

3.2 Steady Climb

We model aircraft climb with the simple steady climb equation for the flight path angle [62], but we correct the thrust for angle of attack since the large amounts of thrust become significant at high angles of attack. The simple correction in eq. (3.3) includes the flight path angle γ, thrust T, total drag D, mass m, angle of attack α, and gravity g.

$$\gamma = \sin^{-1}\left(\frac{T cos\alpha - D}{mg}\right) \tag{3.3}$$

3.3 Transition

To fully characterize the transition path, we could use the x and y components of force and Newton's second law and numerically integrate the acceleration to find the exact path over time. However, this approach becomes infeasible for design optimization. Numerically integrating requires thousands of evaluations, which would make an optimization that normally takes around 20,000 function evaluations or just a few hours, to take several thousand times that, or months to solve.

A simpler approach to full dynamic simulation is to approximate the transition via a circular path and assume that the flight speed, lift, drag, angle of attack, and thrust are constant [63]. Using the dynamic equation for acceleration in a circular path allows us to calculate the circle's radius r, due to the net excess lift L_{net}, as the centrifugal force (eq. (3.4)). With the radius known, the resulting x and y positions are calculated with simple trigonometry in eqs. (3.5) and (3.6) with the rotation being from level, or zero degrees, up to the steady flight path angle γ. The time, t, is calculated by the arc-length distance divided by the flight velocity V_∞ as seen in eq. (3.7).

$$r = \frac{mV^2}{L_{net}} \tag{3.4}$$

$$x = r\cos(\gamma) \tag{3.5}$$

$$y = r\sin(\gamma) + r \tag{3.6}$$

$$t = \frac{r\gamma}{V_\infty} \tag{3.7}$$

3.4 Range

To model range, we used a non-standard formulation in the propulsion frame of reference as opposed to the airframe frame of reference. This was done to increase the convergence rate of the optimization. The more typically used range equation [61] is shown in eq. (3.8), with range R, battery mass m_b, total aircraft mass m_t, battery specific energy e, lift L, drag D, gravity g, and propulsion efficiency η_p. During the optimization, in order to satisfy the constraint on range, the optimization algorithm would choose more lift than was required for steady level flight. This is due to there being an advantage to artificially increase the lift to artificially increase the range, satisfying the range constraint with less energy at cruise though the thrust constraint was violated. Less cruise energy decreases the battery mass, which cascades to change the entire propulsion system. While the optimization would eventually converge with the correct lift and thrust for steady level flight, the number of iterations to do so were much higher than if we modeled range in the propulsion frame of reference.

$$R = \frac{m_b \, e \, 3600 \, \eta_p L}{m_t g \, D} \tag{3.8}$$

This second equation for range, eq. (3.9), is identical to the first assuming the lift equals the total weight and the thrust equals the drag in steady level flight. Alternatively, this equation can be seen as being based directly on the propulsion power output. This second equation, in conjunction with lift and thrust constraints, converges to the same solution as the first equation, but does so in a much more efficient manner. This is due to there being no advantage to artificially augment any part of the equation, thus avoiding the majority of the infeasible design space exploration typical when using the first range equation.

$$R = \frac{m_b \, e \, 3600 \, \eta_p}{T} \tag{3.9}$$

CHAPTER 4. OPTIMIZATION SETUP

In this study, we explore tradeoffs between takeoff distance and cruise speed for the general parameters of the baseline Tecnam p2006t aircraft, but with continuously powered distributed propellers in a retrofit configuration. We chose to keep the airframe, wing, and max takeoff weight unchanged to keep this conceptual study a retrofit of the existing aircraft. Also, to increase efficiency during takeoff and cruise, we include variable pitch propellers, but limit the allowable tip Mach number to Mach 0.8 to stay reasonably within the limits of the XFOIL compressibility correction equations. This configuration, though much less efficient than the NASA X-57 and its optionally powered propulsion units, does not include any discrete design variables other than number of propellers. This enables gradient-based optimization and scalability in terms of design variables.

Using our optimization framework, we investigate only the effects of the propulsion system, while assuming changes in trim drag to be negligible between number of propellers for this comparative study. This assumption is based on an unchanging airframe, including MTOW, and a battery mass distributed to keep the center of gravity unchanged. We vary the number of propellers ranging from 2 until the performance degrades at 32 propellers. We set up the VLM model with 120 control points per half-span. We design the propellers by changing the blade chord, twist, radius, and number of blades while maintaining the same airfoil profile (the Eppler 212 low Reynolds number airfoil). Propellers were modeled as rotating inboard-up due to lower propeller on wing induced drag losses as opposed to outboard-up [64]. In order to model ground roll, transition and climb, and cruise performance, we use three sets of the four variables of RPM, pitch, angle of attack, and battery capacity. We use only one set of variables for the propeller geometry and motor parameters, and size the electronics based on the highest-power case (using a smooth-max function to avoid discontinuities). Battery capacity is modeled as a design variable to avoid an inner convergence loop since the total aircraft mass is required to calculate the battery energy and in turn,

battery mass needed. Energy constraints on the three stages allow the battery mass to converge at the properly sized total value.

4.1 Optimization Algorithm

Gradient based optimization is advantageous for problems with relatively large numbers of design variables. As an example, Rios found that gradient-free algorithms such as Nelder Mead, Particle Swarm, and Genetic Algorithms suffer when there are 30 or more design variables [65]. His test included 22 gradient-free solvers tested on 502 optimization problems. Ning [66] showcases

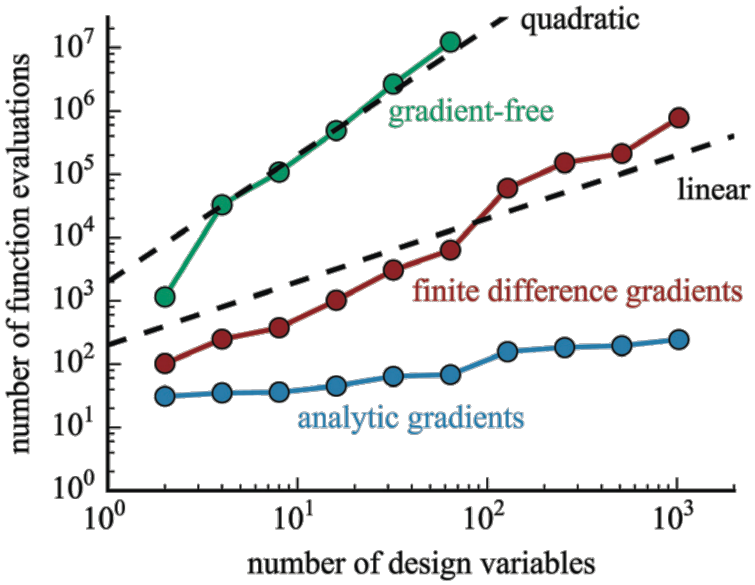

Figure 4.1: Number of function evaluations required to converge optimization as a function of number of design variables. Sparse Nonlinear OPTimizer is used for the gradient-based results and Augmented Lagrangian Particle Swarm Optimizer for the gradient-free results, however similar trends were observed using Sequential Least SQuares Programming (gradient-based) and Non Sorting Genetic Algorithm II (gradient-free). Reference lines for linear and quadratic scaling are also shown. (Image and caption reprinted from "Integrated Design of Downwind Land-based Wind Turbines using Analytic Gradients", by A. Ning, 2016, Wind Energy, 11, 44. Copyright 2016 John Wiley & Sons, Ltd.)

that the number of function evaluations required for convergence for a standard optimization test problem (Rosenbrock Function) scales quadratically for gradient free methods, while it scales only linearly for gradient-based methods using finite differenced gradients. The convergence is relatively constant for gradient-based method using analytic gradients (see fig. 4.1). (Image and caption from Ning et al. [66]). In general, this equates to several orders of magnitude more function evaluations for convergence if one uses gradient-free methods opposed to gradient-based methods for the same number of design variables. For our optimization algorithm, we use one of the same gradient-based algorithms used by Ning, the Sparse Nonlinear OPTimizer (SNOPT) [67], which is a gradient-based sequential quadratic programming method designed for large scale constrained optimization.

While gradient-based methods do have a disadvantage of becoming caught in local minima, this can be overcome by using a multi-start approach. The computational efficiency gains offset the multi-start approach making gradient based optimization a better solution for problems consisting of 30 design variables or more. In the problem explored in this thesis, 35 design variables is the minimum used, which could be increased depending on the radial discretization of the propeller blades. The number of design variables used, as well as the possibility of expanding the optimization framework to include more design variables with wing aerostructural modeling, many differing propellers across the span, and more evaluation points along the path justifies the use of gradient based optimization.

4.1.1 Problem-Specific Optimization Techniques

When using gradient based optimization, there are some ways to help the algorithm more efficiently find converged solutions and satisfy constraints specific to the physics, mathematics, or formulation of the problem. In this subsection we outline four such techniques that were used: splines, fail flags, extra nonlinear constraints, and multi-part optimizations.

The first technique addresses an issue with the BEM model's independent radial sections. In the BEM theory used, each annular control volume is relatively independent of the other annular control volumes. While the optimal propeller design will converge to a continuous variation in

chord and twist consistent with real blade design, directly using the chord and twist at each blade section as design variables will make convergence difficult. This is because each blade section is relatively independent from the rest, taking more function evaluations to find the optimal chord and twist variation. This problem can be overcome by using a spline which connects the sections of the blade through interpolation. We implemented a specific type of spline, an Akima spline[1], which is formulated to avoid overshooting issues common with more standard spline types such as cubic splines. Using this spline, with 4 design variables as the control points along the propeller blades and 8 interpolation points, significantly sped up convergence of the propeller geometry design by as much as 3x.

The second technique used takes advantage of the fail flag in SNOPT. In gradient based optimization, after the gradient is evaluated and a search direction identified, a line search, such as Brent's Method, is conducted along the search direction until the conditions of sufficient decrease (Wolfe Conditions) are met [68]. During the line search, very large steps may be taken, which can take the solution progression into areas that are numerically very difficult from which to return. An example of this is the transition radius in the takeoff equations (see eq. (3.4)). If the line search were to take a step to make the transition radius larger to decrease the required lift in order to satisfy a constraint on lift, it may step too far and make the radius negative. To bring the transition radius back in the positive direction, the radius becomes infinitely large before it becomes positive. To avoid this numerical problem, we set the fail flag to true if the radius or flight path angle (similar issue) becomes negative. The optimization algorithm is then able to stop before it advances too far in an intermediate search direction, allowing it to re-evaluate the gradient and calculate a new search direction in a numerically feasible location.

The third technique uses nonlinear constraints to help the optimization algorithm converge with good solutions. An example of this problem is with the BEM formulation and the airfoil data that includes 360 degrees of rotation. Since the propeller local angle of attack is not known apriori and is only loosely tied to the propeller geometric twist, we cannot impose a bound constraint on the blade angle of attack. This means that very large angles of attack could be encountered for a variable pitch propeller that is operating at a low advance ratio and high pitch. There is a problem that due to the Viterna extrapolation method, the airfoil lift begins to increase after the airfoil has

[1] Akima.jl on BYU FLOW Lab GitHub https://github.com/byuflowlab/Akima.jl.git

stalled. While physically accurate, it is possible for the optimization during an intermediate step to choose a propeller operating at a high pitch and low advance ratio, which is well past stall. If the airfoil local angle of attack is in the region past stall where the lift slope begins to increase, then the gradient will be such that the line search will further increase the angle of attack. By adding the nonlinear constraint on the angle of attack, the solution will be pulled back to operating with normal values for the blade local angle of attack. While one might just strategically truncate the airfoil data to avoid this problem, we include it to keep the full design capabilities to allow for future work such as power regeneration during descent and propeller braking.

Fourth, we used a two part optimization in order to include the number of blades as a design variable. In the BEM model used, varying the number of blades is continuous in terms of solidity, and the noise modeling is the only part that requires integer blade numbers. Because of this, we first optimized the variable blade system without the noise model, then rounded and held the number of blades to an integer value while re-optimizing with the noise model.

4.2 Framework

Figure 4.2 shows the general modeling framework used to evaluate the aircraft performance. In the figure, colors distinguish the design variables (red), models (green) and constraints (blue). The constraints include factors on flight and structural requirements as well as modeling limitations. These include the previously mentioned constraint on the propeller blade local angle of attack α to help with convergence, lift and drag greater than weight, and drag at each respective stage but with thrust allowed to be in excess where needed for takeoff performance, battery sizing, maximum propeller tip speed mach number, maximum SPL, local lift distribution for stall, propeller tip separation to prevent overlapping, MTOW, range, cruise speed, composite failure, and buckling stress.

The design variables used and touched on in fig. 4.2, are expanded in table 4.1, including the upper and lower bounds. The propeller spline control points are discretized into four sections, but the propeller tip chord is allowed to be much smaller. The choice of upper and lower bounds were to help the optimization convergence by limiting the available design space to not include

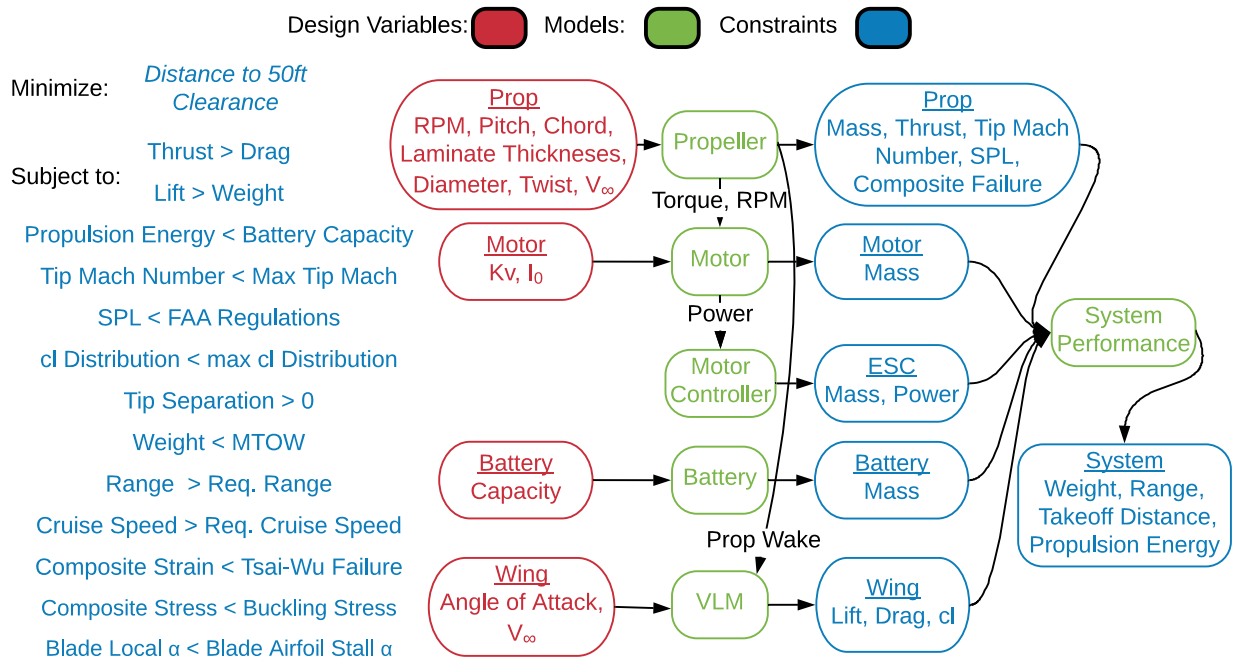

Figure 4.2: Optimization framework with design variables in red, models in green, and outputs in blue. For the multi objective optimization of takeoff distance and cruise speed, we added a speed constraint and ran the analysis framework three times with additional variables for angle of attack, pitch, RPM, and velocity for the cruise and two takeoff parts.

extreme design values. As an example, the lower bound on the wing angles of attack were set to be much lower than the typically converged value, but do not allow for values at which the constraints would always be violated. During development of the final solutions, the upper and lower bounds were updated to reflect this technique, especially when a design variable was at a bound constraint.

Using the Julia programming language, the full propeller and wing, propeller aerostructural, and propulsion system codes run in an average of approximately 0.26 seconds without the noise model and 0.5-3.5 seconds with the noise model depending on the total number of blades. This means warm-started full optimizations usually converge in the order of tens of minutes and non-warm-started optimizations converge in the order of hours.

Table 4.1: Optimization Design Variables and Bounds

Name	Lower Bound	Upper Bound	Number of Variables	Units
Uni Thickness	1.0	100	4	plies
Weave Thickness	1.0	100	4	plies
Prop Chord	0.01	0.8	3	m
Prop Tip Chord	0.001	0.8	1	m
Prop Twist	-0.0	45.0	4	deg
Prop Pitch Accel	-25.0	45.0	1	deg
Prop Pitch Climb	-25.0	45.0	1	deg
Prop Pitch Cruise	-5.0	80.0	1	deg
Prop Radius	0.1	5.0	1	m
Wing AOA Accel	2.0	40.0	1	deg
Wing AOA Climb	5.0	40.0	1	deg
Wing AOA Cruise	0.20	20.0	1	deg
Velocity Accel	5.0	28.0	1	m/s
Velocity Climb	5.0	60.0	1	m/s
Velocity Cruise	20.0	100.0	1	m/s
Prop RPM Accel	200.0	40000.0	1	RPM
Prop RPM Climb	200.0	40000.0	1	RPM
Prop RPM Cruise	100.0	10000.0	1	RPM
Motor Kv	5.0	5000.0	1	RPM/Volt
Motor I_0	0.1	6.0	1	Amps
Batt Mass Accel	0.001	100.0	1	kg
Batt Mass Climb	0.01	100.0	1	kg
Batt Mass Cruise	5.0	1000.0	1	kg
Number Blades	2.0	5.0	1	#

4.3 Baseline Aircraft

As mentioned previously, we chose the Tecnam p2006t aircraft because of the work already being done to exchange the two engines for electric motors [24]. Our intent is to show the conceptual feasibility of electrifying an existing aircraft as a possible near term solution to the urban ODM problem, thus potentially simplifying certification and safety requirements. Table 4.2 shows the main design parameters and limitations of the aircraft.

Because of the relatively low energy density of the electric system, we reduced the conceptual wet useful load to the level of the Cessna 172 in addition to using all of the mass from the engines and fuel for the batteries and electric propulsion system. We chose a 50 km range

Table 4.2: Baseline Tecnam p2006t aircraft [69]

Parameters	**Tecnam p2006t**	**Present Study**
Propulsion Designed For:	Cruise	Short Takeoff
MTOW	1230 kg	1230 kg
Wet Useful Load	257 kg	245 kg
Engines & Fuel	289 kg	0 kg
Propulsion & Battery Allowance	0 kg	301 kg
Cruise Speed	77.3 m/s	22, 45, 67 m/s
Range	1239 km	50 km
Max Power	140 kW	100-600 kW
Flight Path Angle	3.5 deg	7-40 deg
Noise	67 dB(a)	60-76 dB(a)
Wing Area	13.47 m^2	13.47 m^2
Wingspan	11.67 m	11.67 m
Aspect Ratio	10.1	10.1

requirement as the minimum this type of urban transport aircraft would need to begin to be useful, based on the approximate radius of major urban areas such as Dallas, Texas and New York City and also to address the very limited mass available for the propulsion system and battery. Altitude at takeoff for the atmospheric properties was set at sea level, and cruise was set at the minimum allowable altitude of 500 ft (155 m).

CHAPTER 5. RESULTS

For our results, we look at two parameter sweeps, or Pareto fronts, regarding the critical tradeoffs between takeoff distance, cruise speed, and noise. First we explore cruise speed constraints between the minimum speed and recommended cruise speed for the Tecnam p2006t. These nonlinear constraints are formulated to be greater than 50, 100, and 150 mph (22, 45, and 67 m/s) at noise levels less than the Federal Aviation Administration (FAA) regulation of 76 dBa (discussed in section 5.2). Cruise speed affects the takeoff objective by changing the required battery mass which in turn competes with the propulsion mass since the MTOW constraint is always active in the cases tested. Second, we explore noise constraints less than the maximum permissible for the aircraft (76 dBa) at a 100 mph cruise speed (from the previous set). Since those solutions converge to approximately 70 dBa, we then reduce the allowable noise constraint to half the perceived SPL (60 dBa). To show to diverging trend of the curve, we also include 65 dBa and 63 dBa constraints. Noise generation is a byproduct of transferring power from the propulsion system into the surrounding fluid. By constraining the sound power generation, the possible propulsion power output also becomes constrained.

5.1 Cruise Speed Sweep

Figure 5.1 shows the minimum takeoff distance Pareto fronts for varying numbers of propellers and cruise speed constraints. Based on the results of the figure, DEP clearly benefits the takeoff distance with the best high cruise speed case, the 16 propeller case, reducing the takeoff distance to less than half that of the 2 propeller case. Across all cases, excellent theoretical minimum takeoff performance is observed while meeting all other constraints. Predicted noise levels for all cases are below the 76 dBa level. Also, for the 22 m/s case, the cruise speed constraint is not active (indicated by the greater-than symbol) meaning that the converged solutions satisfy the

constraint by achieving a higher cruise speed than the minimum bound constraint. The 2, 4, 8, 16 and 32 propeller cases converge to 34.6, 31.3, 33.1, 31.4 and 25.7 m/s respectively.

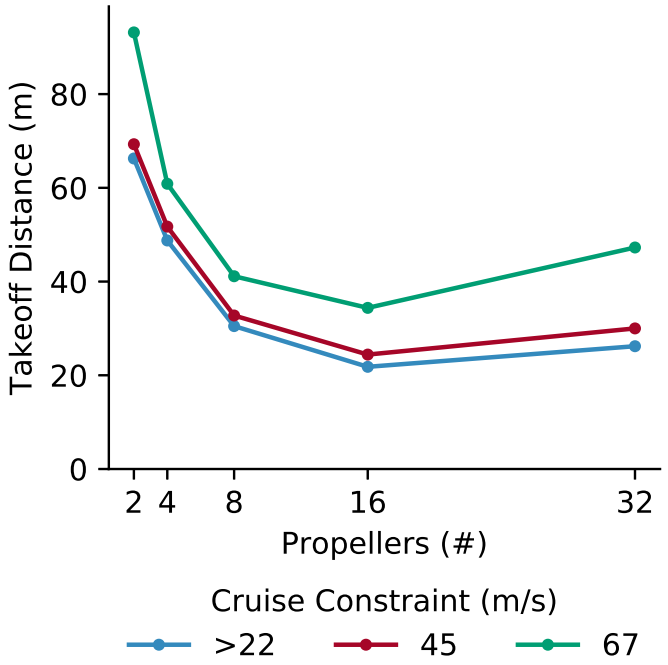

Figure 5.1: Cruise speed and number of propellers effect on optimal takeoff distance to clear a 50 ft obstacle. The 16 propeller case achieves the takeoff distance in less than half that of the 2 propeller case for the cruise speed requirements tested. Greater-than symbol indicates cruise speed constraint was not active.

At these takeoff distances, there are thousands of potential STOL airfield locations within major city limits [23], meaning that DEP applied to STOL urban transport could be a feasibility even in the immediate future. If we next focus on only the ground roll distance part of the takeoff, as shown in fig. 5.2, we can start to make some inferences regarding the takeoff requirements with no obstacle clearance, such as the top of a building. Keeping in mind the limitations of the ground roll distance calculation as described in section 3.1, the number of potential urban locations for full balanced field length takeoff strips raises to the tens of thousands [23]. As will be discussed in the future work section, this study is intended to be a mid-fidelity conceptual feasibility study, indicating further studies in the area are needed to access things such as blown wing stall, landing approach, and powered deceleration.

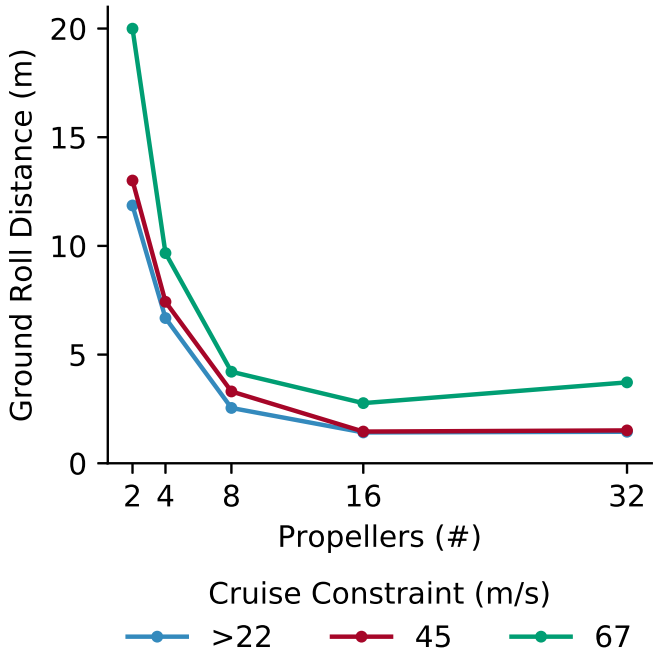

Figure 5.2: Cruise speed and number of propellers effect on resulting ground roll distance.

At the fundamental level of short takeoff, the two main factors in play are increased thrust and increased lift coefficient. These factors are also at the root of the increase in takeoff distance between the 16 and 32 propeller cases seen in figs. 5.1 and 5.2.

5.1.1 Augmented Thrust

The main factor contributing to such a short takeoff distance for all cases shown in fig. 5.1 is total thrust. The net thrust generated is in some cases as high as 80% the aircraft weight (fig. 5.3a). This is due to the relatively large propeller area as well as the inclusion of variable pitch high solidity propellers, which enables much higher thrust at low speeds. This high thrust is also possible, from a battery capacity perspective, due to the short time required for takeoff. The large power required to generate such a large amount of thrust does not significantly contribute to the battery mass. For all cases, the energy for takeoff as described in chapter 4 is less than 1.5% of the total flight energy. The optimizer takes advantage of the highly power-dense electrical components for a short period of time to significantly improve the takeoff objective. This results in an optimum

at the system level, including the tradeoffs between battery mass, propulsion mass, and propulsion efficiency including the propellers' effect on the wing efficiency.

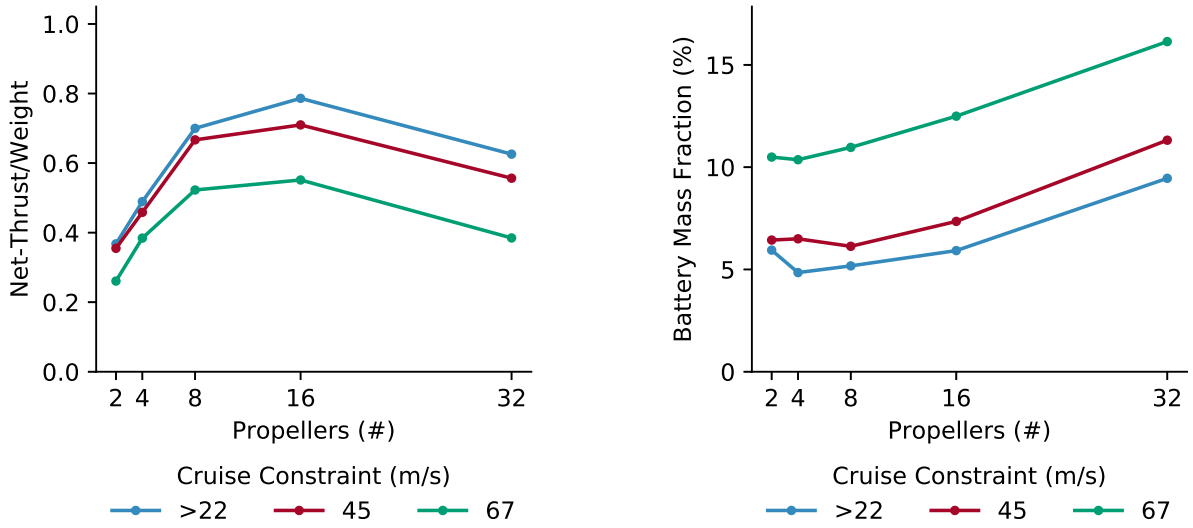

(a) Climb net thrust to weight. Total climb net thrust in excess of 80% of the aircraft weight when the constraints on cruise speed are inactive.

(b) Battery mass fraction of total aircraft mass. Increases with increasing number of propellers to satisfy range constraint at a decreased propulsion efficiency. Also at the expense of propulsion mass with a fixed airframe.

Figure 5.3: Tradeoff between battery mass and propulsion mass, or ability to generate thrust. With MTOW constraint active, propulsion mass must be reduced to allow for extra battery mass to maintain range at the expense of takeoff potential.

After 16 propellers on the span, the takeoff distance increases due to decreased propulsion-efficiency in combination with active cruise speed, range, and MTOW constraints. With increasing number of propeller blades, the propeller efficiency drops due to the modeled tip losses with the 32 propeller, 100 m/s cruise speed case dropping by as much as 10% compared to the 2 propeller case. This decrease in efficiency directly translates to more battery required for cruise, effectively cutting into the available propulsion system mass. With the motors taking as much as 85% of the allowable battery and propulsion mass, a 10% increase in battery mass has the effect of decreasing the possible motor power output by as much as 30%. The tradeoff of battery mass can be seen in fig. 5.3b for cruise speed constraints of 45 m/s and above.

5.1.2 Augmented Lift

Figure 5.4 shows that very large lift coefficients can be achieved with a blown wing system including flaps. Such a high lift coefficient decreases the stall speed, the required takeoff rolling distance, and for a propeller system with relatively constant power, enables greater thrust at the lower speed. This decrease in stall speed is accomplished in part by the propellers increasing the dynamic pressure on the wings as well as thrust vectoring. Thrust vectoring is inherent for a propeller in line with the wing as the angle of attack is increased, but at the cost of decreased forward thrust. The local lift coefficient, normalized by the local velocity, remains below the specified stall constraint of a 2.4 local lift coefficient. The local lift coefficient stall constraint of 2.4 is a surrogate for extended full-span flaps with a zero lift angle of attack of -14 deg for a single slotted flap in 30 degrees deflection [56]. The local lift coefficient of 2.4 is also a 10% margin below the maximum local lift coefficient of the flap configuration chosen.

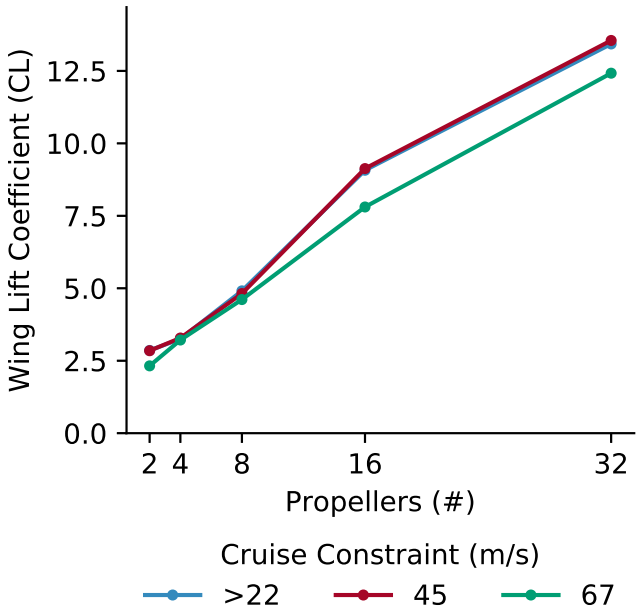

Figure 5.4: Wing lift coefficient in the climb state with an assumed maximum local lift coefficient of 2.4 as a surrogate for extended flaps with a zero lift angle of attack at -14 deg for a single slotted flap with 30 deg deflection [56]. Fully blown configurations increase wing total lift coefficient as normalized by the freestream, though for the highly mass constrained systems, blown velocities and in turn lift coefficient is also constrained due to undersized propulsion systems.

5.1.3 Acceleration Time

With regard to the minimum runway length, typically the balanced field length will be used. The balanced field length is calculated at the velocity for which the accelerate-go and the accelerate-stop distances are equal during the ground roll. In other words, the distance to accelerate then brake to a stop is the same as the distance to accelerate and liftoff. For more traditional aircraft, the reaction time of about 1 second [60] is accounted for in the balanced field length, but is a relatively small portion of the total time. For the retrofit aircraft in this study, the ground roll time for all cases is on the same order of magnitude as the reaction time as seen in fig. 5.5a. This means that in the event of an aborted takeoff, a pilot would be well into the transition and climb phase before reaction would be possible (see fig. 5.5b). To safely abort after a failed takeoff with the aircraft at a steep flight path angle in climb would potentially require enough runway distance to transition to a descent attitude, then descend, land, and finally roll to a stop. The full runway length required to provide an adequate margin of safety for this aircraft may need be much longer than the traditional balanced field length.

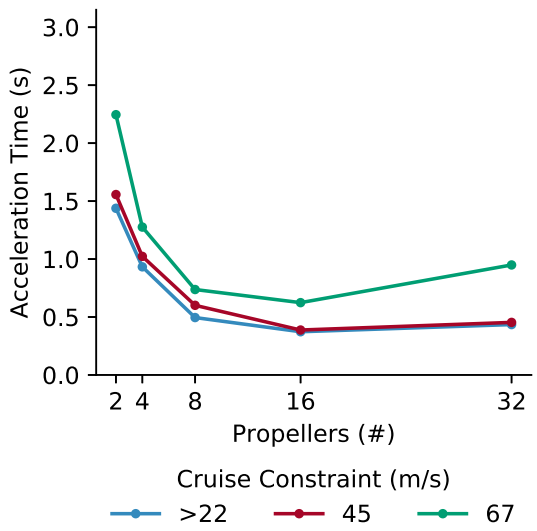

(a) Time during acceleration portion of takeoff.

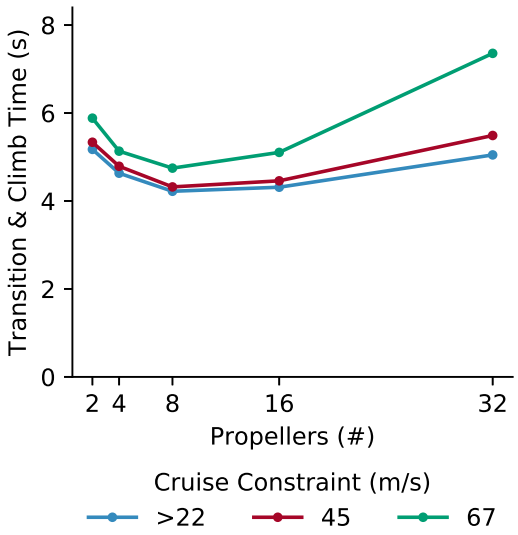

(b) Time during transition and climb to 50 ft portion of takeoff.

Figure 5.5: Time duration for takeoff maneuvers is on the same order of magnitude as a 1 second operator reaction time [60].

5.1.4 Example Propeller Design

To give some insight into the resulting propeller design, we show one propeller from the 8 propeller, 45 m/s cruise case in fig. 5.6. Here we show the two active constraints for the case during climb; composite weave failure on the upper blade and buckling failure on the lower blade. For all of the composite failure modes, a safety factor of 1.5 was included. From this plot, we can make several inferences regarding the propeller design. First, considering the objective of the optimization and physics of flight, the problem has an incentive to reduce the mass in all areas until propeller structural failure constraints become active. Reducing the propeller mass allows greater

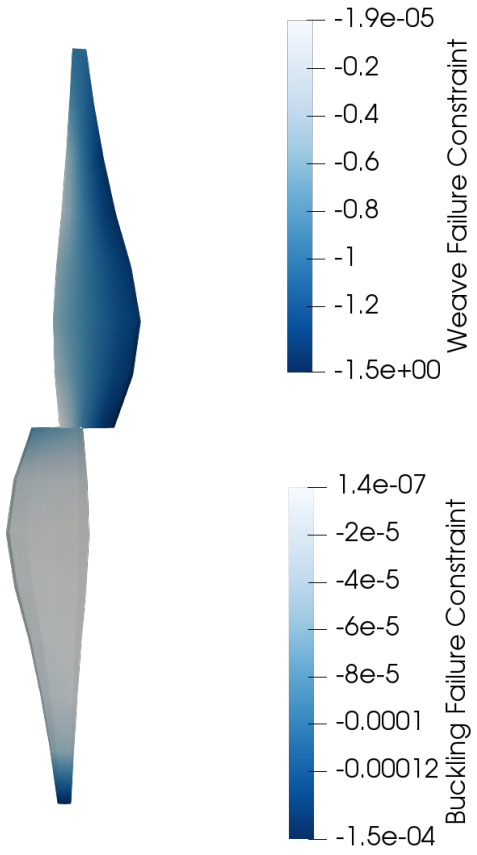

Figure 5.6: Single propeller from the 8 propeller, 45 m/s cruise case with the composite weave failure scaled constraint contour on the upper blade and the buckling failure scaled constraint contour on the lower blade. Constraints are active when zero or positive. Calculated noise for this case was unconstrained and at 71 dBa

motor mass and in turn greater power output potential with the MTOW constraint active. Second, the weave failure constraint is active on the tension side of the blade along the leading edge. With the safety factor constraints active for the corrected material properties during the takeoff portion of the flight, the material property knockdown and safety factors may need to be reconsidered to insure an adequate true safety factor during flight in an urban setting. Third, the optimization tended toward two blades, which after re-optimizing with the integer two blades, still maintained a relatively low solidity design for the outer 50% of the blade. This we attribute to the desirable high propeller efficiency of the case during cruise (82%), which is quite high considering the large net thrust-to-weight produced during takeoff.

Figure 5.7 shows the relative sizes of the optimal propeller diameter with respect to the wing span for the 45 m/s 76 dBa noise case. Between the two and four propeller cases the propeller tip speed is the limiting factor, restricting the propeller diameter. For four propellers, the diameter is nearly as large as the two propeller case, but with four props the possible power output is much greater. Between the four and eight propeller cases, the total mass constraint becomes more dominant in the design space tradeoffs. This limits the power output and in turn the propeller diameter. For cases with more than 8 propellers, the propeller separation constraint becomes active constraining the propellers to be effectively tip to tip. Future work may include modeling overlapping propellers and the resulting performance impacts to allow for staggered, overlapping propellers.

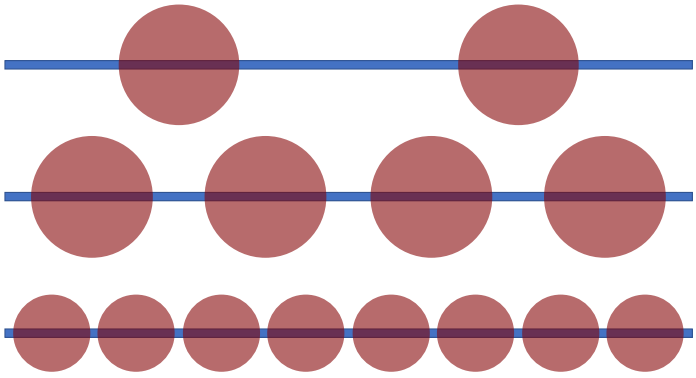

Figure 5.7: Visual depiction of optimal rotor diameters relative to wingspan for the 45 m/s cruise case. For more than 8 propellers, the blades are effectively tip-to-tip across the span.

5.2 Noise Constraint Sweep

Noise is a key element for new aircraft to be of value [70], especially when considering the type of environment in which these aircraft might fly. According to the most recent FAA noise levels advisory for this weight of aircraft[1], the maximum measured SPL is 76 dB(a). According to the Tecnam aircraft manual [69], the maximum SPL for the aircraft, in accordance with the International Civil Aviation Organization is 67.07 dB(a). While we rely on the BPM noise code as an approximation, the maximum takeoff noise for the two propeller case does fall within the correct range at about 67.6 dBa for the 22 m/s cruise speed case increasing to 69.3 dBa for the 67 m/s cruise speed case. In the following results, we chose the noise constraint levels by decreasing the level from the approximate mean of the previous results (70 dBa) by 5 and 10 dBa. When we observed the takeoff distance beginning to diverge at the 60 dBa constraint, we included the 63 dBa constraint to better quantify the diverging trend. The noise we report for this simple conceptual design study is calculated as the maximum SPL in flyover at 50 feet altitude relative to a ground observer in line with the aircraft center axis.

Figure 5.8 shows the effect of the propeller noise constraint on the takeoff distance with varying numbers of propellers. For all of the cases tested, as noise decreased, there was a divergent increase in the takeoff distance. Focusing on the best case with respect to the constraints, 8 propeller case, there was only a 15% increase in the takeoff distance between propeller noise constraints of less than 76 (converged to 71) dBa and 65 dBa, which translates to about 3/4 of the perceived noise level. However, for very strenuous noise constraints, the trend becomes divergent with an additional 50% increase increase in takeoff distance between noise constraints of 65 and 60 dBa.

As previously discussed in section 2.3, the design space with varying number of propellers is non-intuitive. The full design of the propellers needs to be included to get a more accurate prediction on the noise produced. Moving from the 8 propeller to 16 propeller cases, it would appear that an exponential trend in takeoff distance would continue with 32 propellers, but the opposite is true due to the propellers' design and operating condition. To go further into the effects

[1]FAA Advisory Circulars https://www.faa.gov/airports/resources/advisory_circulars, accessed 6/26/18

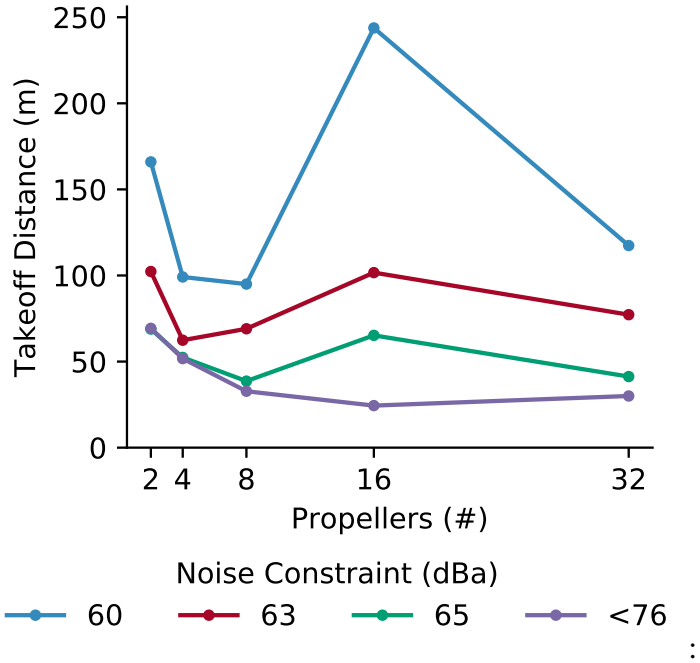

Figure 5.8: Noise constraint effects on optimal takeoff distance with varying numbers of propellers. Decreasing the propeller noise constraint significantly increases takeoff distance. This analysis differs from section 5.1 with a fixed 45 m/s cruise speed constraint and varying propeller noise constraint. Less-than symbol indicates noise constraint was not active

of the noise constraint, we focus on thrust and lift coefficient, the two main factors that decrease takeoff field length as discussed earlier in section 5.1.

5.2.1 Noise Constrained Thrust

While the optimal propeller diameter and solidity remain relatively constant for a given number of propellers under the varying noise constraint, the tip speed for more propellers decreases sharply. As discussed in section 2.3, to achieve a similar SPL between many high solidity propellers and a few low solidity propellers, the propeller tip speed of the greater number of propellers must be significantly decreased. From the thrust coefficient equation $T = C_T \rho n^2 D^4$, with a relatively constant coefficient of thrust C_T, air density ρ, and diameter D but changing rotation rate n, the generated thrust is decreased in an n^2 manner due to decreased tip speed. The effects of this can be seen in fig. 5.9a with the greater number of propellers experiencing a much greater penalty

on thrust to weight with decreasing noise constraint. However, even down to a noise constraint of 63 dBa, the 8 propeller takeoff distance is still below 100 m.

5.2.2 Noise Constrained Lift Coefficient

With the decrease in available thrust due to the tip speed constraint, the propeller wake velocity is also decreased. This decreases the dynamic pressure relative to a case with a higher blown velocity, and in turn, decreases the wing lift coefficient. As seen in fig. 5.9b for the 8 propeller case, the lift coefficient is decreased from 5.0 at the 76 dBa constraint level to 3.5 at the 63 dBa constraint level.

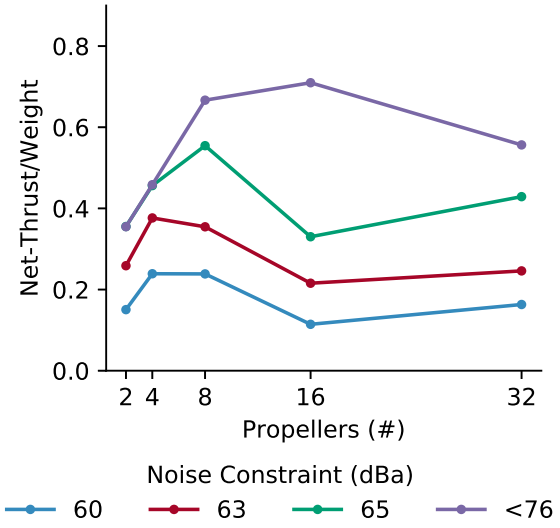

(a) Climb net thrust to weight with noise constraint effects, 45m/s cruise, compare fig. 5.3a. Total climb thrust in excess of 70% of the aircraft weight when the constraints on cruise speed are inactive.

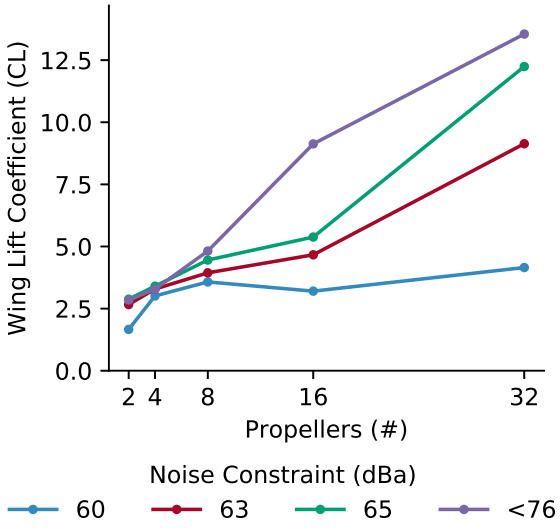

(b) Wing lift coefficient in the climb state, compare fig. 5.4. Noise constraints significantly decrease the ability of more propellers to produce excess dynamic pressure and in turn augmented lift coefficients.

Figure 5.9: Noise constraint effects on thrust and augmented lift. Decreasing noise allows for less thrust, less induced velocity, and in turn less lift augmentation.

With decreased available thrust and decreased wing lift coefficient, it takes longer to accelerate the aircraft mass to a higher takeoff speed than before as well as to climb to the required height. However, as previously mentioned and as also shown in fig. 5.10, (a close up of the 16

propeller case) this trend is divergent and shows relatively little effect on the takeoff distance until the noise constraint dips below 65 dBa.

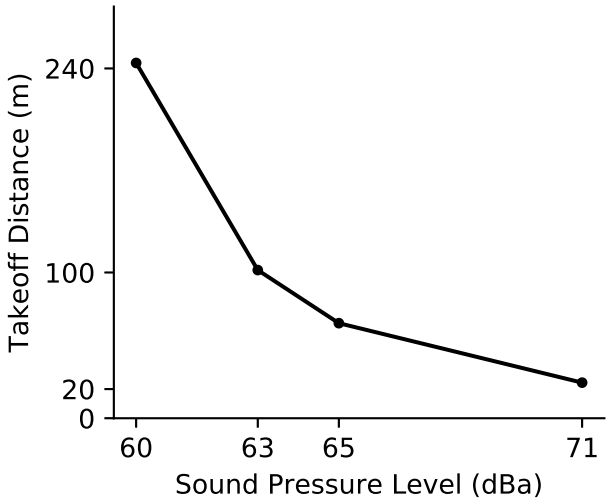

Figure 5.10: Takeoff distance for the 16 propeller, 45 m/s cruise case with varying noise constraint shows relatively small effect on performance for noise levels between 71 and 65 dBa.

CHAPTER 6. SUMMARY

In this study, we explored tradeoffs between takeoff distance and cruise speed for the general parameters of the baseline Tecnam p2006t aircraft with continuously powered distributed electric propulsion (DEP) in a retrofit configuration. We chose to keep the airframe, wing, and max takeoff weight unchanged to keep this conceptual study a retrofit of the existing aircraft. Also, to increase efficiency during takeoff and cruise, we included variable pitch propellers, but limited the allowable tip Mach number to Mach 0.8 to stay reasonably within the limits of XFOIL's compressibility correction. This configuration, though much less efficient than the NASA X-57 and its optionally powered propulsion units, does not include any discrete design variables other than number of propellers. This enables gradient-based optimization and scalability in terms of number of design variables.

Using our optimization framework, we investigated only the effects of the propulsion system, while assuming trim drag to be negligible between number of propellers for this comparative study. This assumption was based on an unchanging airframe, including maximum takeoff weight, and a battery mass distributed to keep the center of gravity unchanged. We varied the number of propellers ranging from 2 propellers until the performance began to degrade between 16 and 32 propellers. We set up the wing vortex lattice method model with 120 control points per wing half-span. We optimized the propellers by changing the blade chord, twist, radius, and number of blades while maintaining the same airfoil profile (the Eppler 212 low Reynolds number airfoil). Propellers were modeled as rotating inboard-up due to lower propeller on wing induced drag losses as opposed to outboard-up [64]. In order to model ground roll, transition and climb, and cruise performance, we used three sets of the four variables of RPM, pitch, angle of attack, and battery capacity. We used only one set of variables for the propeller geometry and motor parameters, and sized the electronics based on the highest-power case (using a smooth-max function to avoid discontinuities). Battery capacity was modeled as a design variable to avoid an inner convergence

loop since the total aircraft mass is required to calculate the battery energy, and in turn, battery mass needed. Energy constraints on the three stages allowed the battery mass to converge at the properly sized total battery mass.

We explored how continuously powered distributed propulsion can reduce takeoff distance while maintaining the mass and sound constraints of the original aircraft at a minimum 50 km range, a variety of cruise speeds, and a variety of decreased noise constraints. To model and explore the design space we used a set of validated models including a blade element momentum (BEM) method, a vortex lattice method (VLM), linear beam finite element analysis (FEA), classical laminate theory (CLT), composite failure, empirically-based blade BPM (Brooks, Pope, and Marcolini) noise modeling, motor mass and motor controller empirical mass models, and nonlinear gradient-based optimization. In this conceptual design study, we found that a fully blown wing with 16 propellers could reduce the takeoff distance by over 50% when compared to the optimal 2 propeller case. This resulted in a conceptual minimum takeoff distance of 20.5 meters to clear a 50 ft (15.24 m) obstacle. We found that when decreasing the allowable noise to 60 dBa, the fully blown 8 propeller case performed the best with a 43% reduction in takeoff distance compared to the optimal 2 propeller case. The increase in takeoff distance due to noise constraints was divergent with relatively little effect until the noise-performance tradeoffs become significant at levels below 65 dBa for all cases tested. For the 8 propeller case at the 65 dBa constraint (70% of the perceived sound pressure level) there was only a 15% increase in the takeoff distance. This case yielded a total conceptual takeoff distance of approximately 37 m. Further reducing allowable noise to a 60 dBa constraint (50% perceived noise reduction) resulted in an additional 2.4x increase in takeoff distance for the 8 propeller case, pushing the takeoff distance to just over 90 m.

6.1 Conclusions

We concluded that based on the results of this study, a distributed electric propulsion short takeoff and landing fixed wing aircraft may be an immediately implementable candidate for the on demand mobility (ODM) urban air transport problem and warrants more work in the area. The retrofit propulsion system in this study conceptually enabled the existing Tecnam p2006t to achieve

takeoff distances which would open thousands of potential options for urban air taxi runways. When cruise speed and noise constraints are also included, the best fully blown DEP system was still able to outperform the more traditional 2 propeller system for the short range requirement modeled and still achieve a takeoff distance of less than 100 meters.

6.2 Future Work

Future work which could significantly benefit this concept are in the areas of design and certification requirements. On the design side, work could include more design freedom to completely change an aircraft configuration for a given mission. Some possibilities include modeling propeller design that varies along the wingspan as well as including propellers above or below the chord line to further influence the lift distribution and system efficiency. Optionally powered and overlapping units, as well as including aircraft constraints on things such as brakes for landing, fuselage structure for increased wing loading, stability, control, and full wing redesign could be included. The noise of the electric motors, lifting surfaces, and control surfaces, could be added into the noise model. The second order motor model including heat transfer could be included as well as a time-dependent battery model. Additionally, one might model the landing portion of the flight including a final landing approach suggested by Patterson et al. [18], expand on the powered deceleration as modeled by Courtin et al. [23], and model the optimal flight path similar to work by Hwang [8].

On the certification side, which is a critical component to the potential implementation of this concept, there is significant work that would need to be done to access the safety, flight requirements, and potential changes to stall regulations similar to those also suggested by Patterson [18] as well as required total field length when the balanced field length is so short. Other areas may address safety requirements with multiple partially independent propulsion units, urban gusts and building wind factors, and required infrastructure.

6.3 Code

The final code and data used to produce this thesis will be available on the BYU FLOW Lab website[1] following a six month embargo period.

[1] FLOW Lab http://flow.byu.edu

REFERENCES

[1] Colas, D., Roberts, N. H., and Suryakumar, V. S., 2018. "HALE multidisciplinary design optimization part I: Solar-powered single and multiple-boom aircraft." In *2018 Aviation Technology, Integration, and Operations Conference*, American Institute of Aeronautics and Astronautics. 1

[2] Gohardani, A. S., Doulgeris, G., and Singh, R., 2011. "Challenges of future aircraft propulsion: A review of distributed propulsion technology and its potential application for the all electric commercial aircraft." *Progress in Aerospace Sciences,* **47**(5), Jul, pp. 369–391. 2

[3] Griffith, A., 1954. Improvements relating to aircraft and aircraft engine installations. United Kingdom Patent, 720,394. 2

[4] Flittie, K., and Curtin, B., 1998. "Pathfinder solar-powered aircraft flight performance." In *23rd Atmospheric Flight Mechanics Conference*, AIAA. 2

[5] Yaros, S., Sexstone, M., Huebner, L., Lamar, J., McKinley., R., and Torres, A., 1998. Synergistic airframe–propulsion interactions and integrations: a white paper prepared by the 1996–1997 langley aeronautics technical committee Tech. Rep. TM-1998-207644, NASA, Mar. 2

[6] Noll, T. E., Ishmael, S. D., Henwood, B., Perez-Davis, M. E., Tiffany, G. C., Madura, J., Gaier, M., Brown, J. M., and Wierzbanowski, T., 2007. "Technical findings, lessons learned, and recommendations resulting from the helios prototype vehicle mishap." NASA Langley Research Center Hampton VA. 2

[7] Moore, M. D., 2006. "The third wave of aeronautics: On-demand mobility." In *SAE Technical Paper Series*, SAE Transactions, pp. 713–722. 2

[8] Hwang, J. T., and Ning, A., 2018. "Large-scale multidisciplinary optimization of an electric aircraft for on-demand mobility." In *2018 AIAA/ASCE/AHS/ASC Structures, Structural Dynamics, and Materials Conference*, American Institute of Aeronautics and Astronautics. 2, 3, 63

[9] Stoll, A. M., Bevirt, J., Moore, M. D., Fredericks, W. J., and Borer, N. K., 2014. "Drag reduction through distributed electric propulsion." In *14th AIAA Aviation Technology, Integration, and Operations Conference*, AIAA. 2

[10] Borer, N. K., Derlaga, J. M., Deere, K. A., Carter, M. B., Viken, S., Patterson, M. D., Litherland, B., and Stoll, A., 2017. "Comparison of aero-propulsive performance predictions for distributed propulsion configurations." In *55th AIAA Aerospace Sciences Meeting*, American Institute of Aeronautics and Astronautics. 2

[11] Harish, A., Perron, C., Bavaro, D., Ahuja, J., Ozcan, M., Justin, C. Y., Briceno, S. I., German, B. J., and Mavris, D., 2016. "Economics of advanced thin-haul concepts and operations." In *16th AIAA Aviation Technology, Integration, and Operations Conference*, American Institute of Aeronautics and Astronautics. 2

[12] Patterson, M. D., and German, B., 2014. "Conceptual design of electric aircraft with distributed propellers: Multidisciplinary analysis needs and aerodynamic modeling development." In *52nd Aerospace Sciences Meeting*, American Institute of Aeronautics and Astronautics. 2

[13] Deere, K. A., Viken, J. K., Viken, S., Carter, M. B., Wiese, M., and Farr, N., 2017. "Computational analysis of a wing designed for the x-57 distributed electric propulsion aircraft." In *35th AIAA Applied Aerodynamics Conference*, American Institute of Aeronautics and Astronautics. 2

[14] Dubois, A., van der Geest, M., Bevirt, J., Christie, R., Borer, N. K., and Clarke, S. C., 2016. "Design of an electric propulsion system for SCEPTOR's outboard nacelle." In *16th AIAA Aviation Technology, Integration, and Operations Conference*, American Institute of Aeronautics and Astronautics. 2

[15] Clarke, S., Redifer, M., Papathakis, K., Samuel, A., and Foster, T., 2017. "X-57 power and command system design." In *2017 IEEE Transportation Electrification Conference and Expo (ITEC)*, IEEE, pp. 393–400. 2

[16] Papathakis, K. V., Schnarr, O. C., Lavelle, T. M., Borer, N. K., Stoia, T., and Atreya, S., 2018. "Integration concept for a hybrid-electric solid-oxide fuel cell power system into the x-57 "maxwell"." In *2018 Aviation Technology, Integration, and Operations Conference*, American Institute of Aeronautics and Astronautics. 2

[17] Falck, R. D., Chin, J., Schnulo, S. L., Burt, J. M., and Gray, J. S., 2017. "Trajectory optimization of electric aircraft subject to subsystem thermal constraints." In *18th AIAA/ISSMO Multidisciplinary Analysis and Optimization Conference*, American Institute of Aeronautics and Astronautics. 3

[18] Patterson, M. D., and Borer, N. K., 2017. "Approach considerations in aircraft with high-lift propeller systems." In *17th AIAA Aviation Technology, Integration, and Operations Conference*, American Institute of Aeronautics and Astronautics. 3, 37, 63

[19] Holmes, B. J., 2016. "A vision and opportunity for transformation of on-demand air mobility." In *16th AIAA Aviation Technology, Integration, and Operations Conference*, American Institute of Aeronautics and Astronautics. 3

[20] Antcliff, K. R., Moore, M. D., and Goodrich, K. H., 2016. "Silicon valley as an early adopter for on-demand civil VTOL operations." In *16th AIAA Aviation Technology, Integration, and Operations Conference*, American Institute of Aeronautics and Astronautics. 3

[21] Holmes, B. J., Durham, M. H., and Tarry, S. E., 2004. "Small aircraft transportation system concept and technologies." *Journal of Aircraft,* **41**(1), jan, pp. 26–35. 3

[22] Moore, K. R., and Ning, A., 2018. "Distributed electric propulsion effects on existing aircraft through multidisciplinary optimization." In *2018 AIAA/ASCE/AHS/ASC Structures, Structural Dynamics, and Materials Conference*, American Institute of Aeronautics and Astronautics. 3, 14

[23] Courtin, C., Burton, M. J., Yu, A., Butler, P., Vascik, P. D., and Hansman, R. J., 2018. "Feasibility study of short takeoff and landing urban air mobility vehicles using geometric programming." In *2018 Aviation Technology, Integration, and Operations Conference*, American Institute of Aeronautics and Astronautics. 4, 50, 63

[24] Borer, N. K., Patterson, M. D., Viken, J. K., Moore, M. D., Bevirt, J., Stoll, A. M., and Gibson, A. R., 2016. "Design and performance of the NASA SCEPTOR distributed electric propulsion flight demonstrator." In *16th AIAA Aviation Technology, Integration, and Operations Conference*, American Institute of Aeronautics and Astronautics. 5, 47

[25] , 1976. Us standard atmosphere 1976 Tech. Rep. NASA-TM-X-74335, NASA. 7

[26] Drela, M., 2014. *Flight Vehicle Aerodynamics*. MIT Press, Feb. 7

[27] Ning, A., 2014. "A simple solution method for the blade element momentum equations with guaranteed convergence." *Wind Energy,* **17**(9), Sep, pp. 1327–1345. 8

[28] Glauert, H., 1935. "Airplane propellers. in: Aerodynamic theory." Vol. 4. Springer, Berlin, Heidelberg, pp. 169–360. 9

[29] Alvarez, E. J., and Ning, A., 2018. "Development of a vortex particle code for the modeling of wake interaction in distributed propulsion." In *2018 Applied Aerodynamics Conference*, American Institute of Aeronautics and Astronautics. 10, 32

[30] Epema, H., 2017. "Wing optimisation for tractor propeller configurations." Master's thesis, Delft University of Technology, Jun. viii, 10, 14, 15, 32

[31] Veldhuis, L. L. M., 2005. "Propeller wing aerodynamic interference." PhD thesis, Technical University of Delft, June. 10, 11, 27, 28, 32

[32] Ning, S. A., 2013. AirfoilPrep.py documentation: Release 0.1.0 Tech. rep., sep. 12

[33] Du, Z., and Selig, M., 1998. "A 3-d stall-delay model for horizontal axis wind turbine performance prediction." In *1998 ASME Wind Energy Symposium*, American Institute of Aeronautics and Astronautics. viii, 12

[34] Eggers, A. J., Chaney, K., and Digumarthi, R., 2003. "An assessment of approximate modeling of aerodynamic loads on the UAE rotor." In *ASME 2003 Wind Energy Symposium*, ASME. 12

[35] Viterna, L. A., and Janetzke, D. C., 1982. Theoretical and experimental power from large horizontal-axis wind turbines Tech. rep., Sep. 12

[36] Tingey, E. B., and Ning, A., 2017. "Trading off sound pressure level and average power production for wind farm layout optimization." *Renewable Energy,* **114**, Dec, pp. 547–555. 15

[37] Brooks, T. F., and Marcolini, M. A., 1986. "Airfoil tip vortex formation noise." *AIAA Journal,* **24**(2), Feb, pp. 246–252. 15

[38] Brooks, T. F., Pope, D. S., and Marcolini, M. A., 1989. Airfoil self-noise and prediction Tech. Rep. 1218, NASA, July. 15

[39] Ning, S. A., 2013. pBEAM documentation: Release 0.1.0 Tech. rep., Sep. 20

[40] Kassapoglou, C., 2013. "Design and analysis of composite structures: With applications to aerospace structures." John Wiley & Sons, Apr, pp. 55–63. 21, 23

[41] Fukunaga, H., and Sekine, H., 1993. "Optimum design of composite structures for shape, layer angle and layer thickness distributions." *Journal of Composite Materials,* **27**(15), Dec, pp. 1479–1492. 23

[42] Blasques, J. P., Berggreen, C., and Andersen, P., 2010. "Hydro-elastic analysis and optimization of a composite marine propellerå." *Marine Structures,* **23**(1), Jan, pp. 22–38. 23

[43] Tsai, S. W., and Wu, E. M., 1971. "A general theory of strength for anisotropic materials." *Journal of Composite Materials,* **5**(1), Jan, pp. 58–80. 23

[44] Gol'denblat, I. I., and Kopnov, V. A., 1966. "Strength of glass-reinforced plastics in the complex stress state." *Polymer Mechanics,* **1**(2), pp. 54–59. 23

[45] Tomblin, J., Sherraden, J., Seneviratne, W., and Raju, K., 2002. "Advanced general aviation transport experiments. a–basis and b–basis design allowables for epoxy–based prepreg toray t700gc-12k-31e/# 2510 unidirectional tape." *National Institute for Aviation Research Wichita State University, Wichita, Kansas*. 23

[46] Tomblin, J., Sherraden, J., Seneviratne, W., and Raju, K., 2002. "Advanced general aviation transport experiments. abasis and bbasis design allowables for epoxy based prepreg: Toray t700sc-12k-50c/#2510 plain weave fabric." *National Institute for Aviation Research Wichita State University, Wichita, Kansas*. 23

[47] Johnson, A., 1994. "Structural component design techniques." In *Handbook of Polymer Composites for Engineers*. Elsevier, pp. 136–180. 24

[48] Resor, B., 2013. Definition of a 5mw/61.5m wind turbine blade reference model. Tech. rep., Apr. viii, 24, 25

[49] Wilson, R. E., Lissaman, P. B. S., and Walker, S. N., 1976. *Aerodynamic Performance of Wind Turbines*. 24

[50] Jonkman, J., Butterfield, S., Musial, W., and Scott, G., 2009. Definition of a 5-MW reference wind turbine for offshore system development Tech. rep., Feb. 26

[51] Lan, C. E., 1974. "A quasi-vortex-lattice method in thin wing theory." *Journal of Aircraft,* **11**(9), sep, pp. 518–527. 27

[52] Ning, A., Flanzer, T., and Kroo, I., 2011. "Aerodynamic performance of extended formation flight." *Journal of Aircraft,* **48**(3), May, pp. 855–865. 28

[53] Alba, C., Elham, A., German, B., and Veldhuis, L. L., 2017. "A surrogate-based multi-disciplinary design optimization framework exploiting wing-propeller interaction." In *18th AIAA/ISSMO Multidisciplinary Analysis and Optimization Conference*, American Institute of Aeronautics and Astronautics. 28

[54] Hunsaker, D., and Snyder, D., 2006. *A Lifting-Line Approach to Estimating Propeller/Wing Interactions*. American Institute of Aeronautics and Astronautics, 2017/12/14. 28

[55] Veldhuis, L. L. M., 2004. "Review of propeller-wing aerodynamic interference." In *International Congress of the Aeronautical Sciences*. 28, 32

[56] Abbott, I. H., and von Doenhoff, A. E., 2012. "Theory of wing sections: Including a summary of airfoil data." Courier Corporation, Apr, ch. High-Lift Devices, pp. 188–247. x, 29, 53

[57] Drela, M., 2007. *First Order DC Electric Motor Model*. MIT Aero and Astro, Cambridge Massachusetts, Feb. 33, 34

[58] Drela, M., 2007. *Second Order DC Electric Motor Model*. MIT Aero and Astro, Cambridge Massachusetts, February. 33

[59] Mikhaylik, Y. V., Kovalev, I., Schock, R., Kumaresan, K., Xu, J., and Affinito, J., 2010. "High energy rechargeable li-s cells for EV application: Status, remaining problems and solutions." ECS. 36

[60] TSTA, 2016. Pilot guide to takeoff safety Tech. rep., FAA. x, 37, 54

[61] Anderson, J., 2015. "Introduction to flight." McGraw-Hill Higher Education, Feb, pp. 447–455,469–474. 38, 40

[62] Anderson, 1999. "Aircraft performance & design." Tata McGraw-Hill Education, pp. 265–267. 38

[63] Mair, W. A., and Birdsall, D. L., 1992. "Take-off and landing performance." In *Aircraft Performance*. Cambridge University Press, pp. 119–161. 39

[64] Kroo, I., 1986. "Propeller-wing integration for minimum induced loss." *Journal of Aircraft,* **23**(7), Jul, pp. 561–565. 41, 61

[65] Rios, L. M., and Sahinidis, N. V., 2012. "Derivative-free optimization: a review of algorithms and comparison of software implementations." *Journal of Global Optimization,* **56**(3), jul, pp. 1247–1293. 42

[66] Ning, A., and Petch, D., 2016. "Integrated design of downwind land-based wind turbines using analytic gradients." *Wind Energy,* **19**(12), Feb, pp. 2137–2152. 42, 43

[67] Gill, P. E., Murray, W., and Saunders, M. A., 2002. "SNOPT: An SQP algorithm for largescale constrained optimization." *SIAM Journal on Optimization,* **12**(4), pp. 979–1006. 43

[68] Nocedal, J., and Wright, S., 2006. *Numerical Optimization*. Springer Science & Business Media, Dec. 44

[69] TECNAM AIRCRAFT, 2010. *P2006T Aircraft Flight Manual*., 2 ed. 29536 Flying Fortress Lane, Suite 1 Sebring, FL 33870, Nov. vi, 48, 57

[70] Moore, M. D., 2014. "Misconceptions of electric aircraft and their emerging aviation markets." In *52nd Aerospace Sciences Meeting*, American Institute of Aeronautics and Astronautics. 57

APPENDIX A. STEADY CLIMB TRADEOFF STUDY

In a purely conceptual light in order to build insight into the progression of the optimization results, we modeled steady climb with lift induced drag and a constant viscous drag to explore the tradeoffs with climb. Building on the previous section for steady climb, we derive an equation for airspeed (equation A.3) composed of equations A.1 and A.2. This is important for calculating flight path angle, thrust, and power tradeoffs. All of the values in equation A.3 are known except the takeoff distance d (the horizontal distance after roll to get to altitude). The takeoff distance can be calculated by using the trigonometric relation in equation A.5 with A.4 to get the final equation A.6. Equations A.7 and A.8 show the calculation of drag from lift and the parasitic drag. This set of implicit equations must be iteratively solved to calculate the airspeed, V_∞, for a given set of parameters. However, the process is computationally inexpensive and gives significant insight into the tradeoffs involved with steady state climb.

$$\cos(\gamma) = \cos\left(\tan^{-1}\left(\frac{h}{d}\right)\right) = \frac{1}{\sqrt{1+(\frac{h}{d})^2}} \tag{A.1}$$

$$L = C_L\frac{1}{2}\rho V_\infty^2 S_{\text{ref}} = mg\cos(\gamma) \tag{A.2}$$

$$V_\infty = \sqrt{\frac{2mg}{C_L\rho S_{ref}\sqrt{(1+\frac{h}{d})^2}}} \tag{A.3}$$

$$\tan(\gamma) = \frac{h}{d} \tag{A.4}$$

$$\tan\left(\sin^{-1}\left(\frac{T-D}{mg}\right)\right) = \sqrt{\left(\frac{mg}{T-D}\right)^2 - 1} \tag{A.5}$$

$$d = h\sqrt{\left(\frac{mg}{T-D}\right)^2 - 1} \tag{A.6}$$

$$C_D = \frac{C_L^2}{\pi e_{wing} AR} + C_{Dp} \tag{A.7}$$

$$D = C_D \frac{1}{2} \rho V_\infty^2 S_{ref} \tag{A.8}$$

The tradeoff during climb can be summarized in the following three figures. First, in fig. A.1, the flight path angle is predominantly based on the aircraft thrust. Increasing the lift coefficient decreases the net thrust some, but not in a significant manner with respect to the flight path angle.

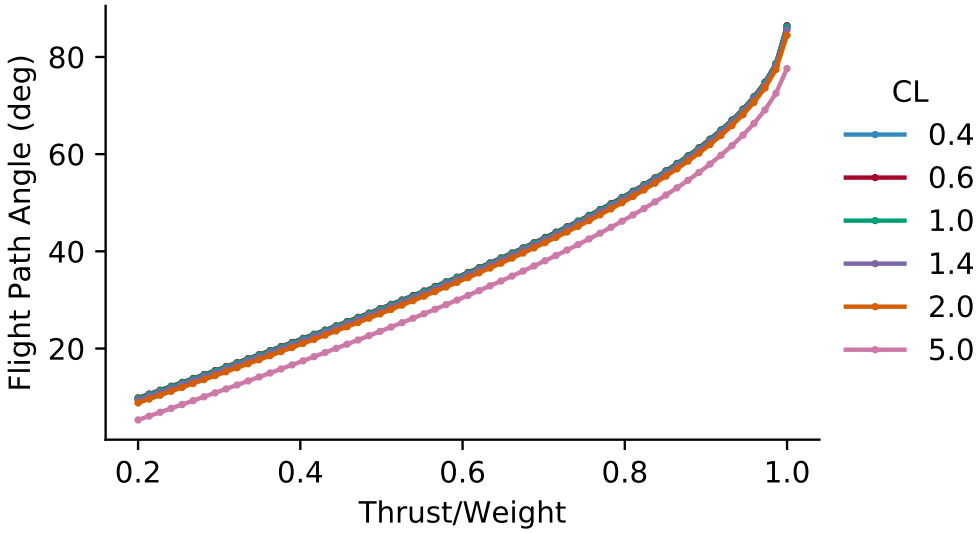

Figure A.1: Thrust is the major factor when determining the flight path angle. Increasing lift coefficient increases the induced drag which decreases the net thrust.

Second, in fig. A.2, as the lift coefficient increases, the power to fly a given flight path angle decreases substantially. An example of this is if one were to fly at a flight path angle of 45 degrees. It takes half the power to fly that path with a lift coefficient of 1.4 as opposed to a lift coefficient of 0.4.

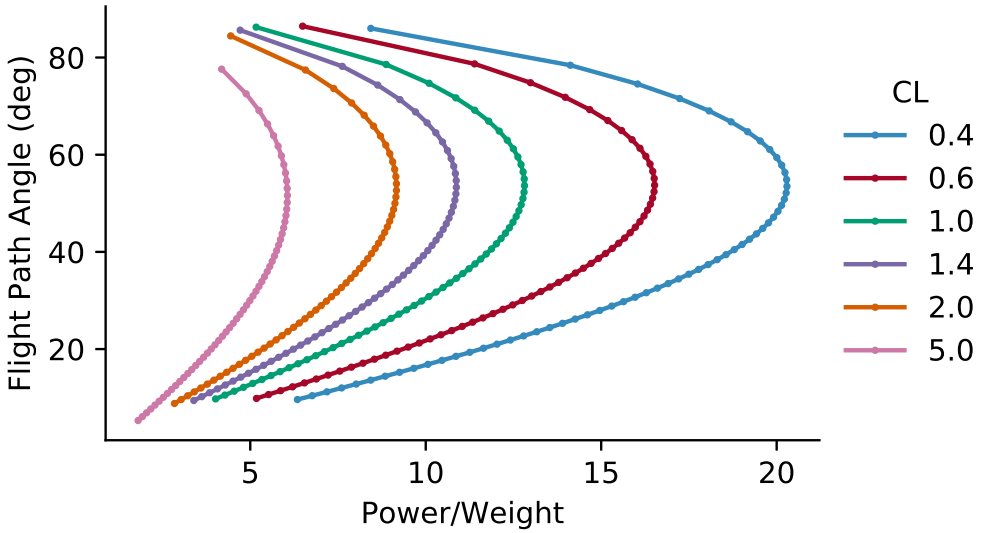

Figure A.2: Lift coefficient plays a significant role in the power required for a given flight path angle. Increasing from 0.4 to 1.4 halves the amount of power required for a 45 degree flight path angle.

Third, in fig. A.3, as the lift coefficient increases, the total energy for the maneuver also increases. This is due to the quadratic increase in induced drag. However, if the drag does not increase quadratically by the use of high lift devices, powered or unpowered, there may be less of a penalty on the total energy.

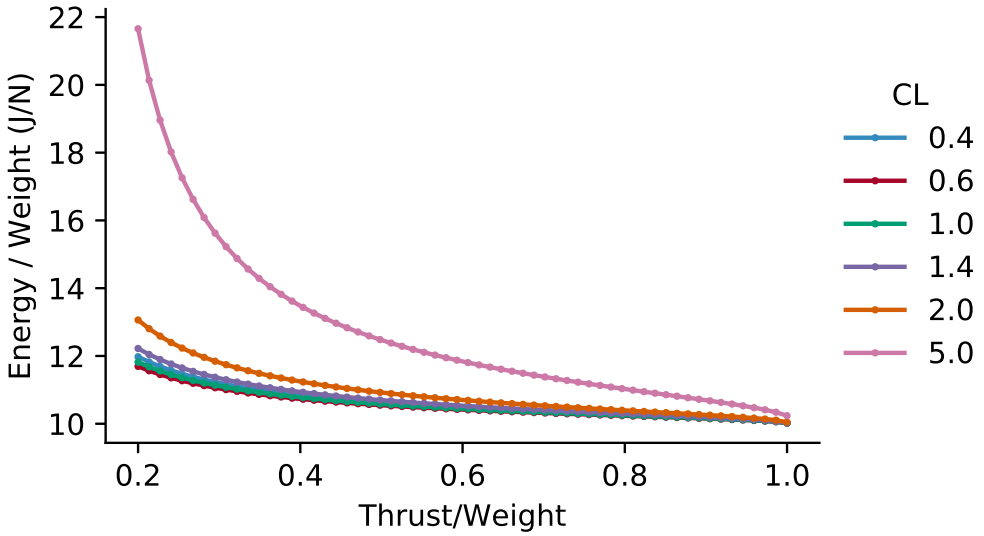

Figure A.3: Increasing the lift coefficient decreases total energy for the climb until the maximum net power is achieved. A lift coefficient of 0.6 is the best for the cases shown here.

For aircraft design, these tradeoffs give insight into how one would design a propulsion system, or determine if optimization results are reasonable. To decrease the power required for a given desired flight path angle, one must increase the lift coefficient, and to minimize the energy for the climb, one must decrease the drag until the maximum net power is achieved.